

BASIC SCIENCES



TF-FVIIa PAR2- β -Arrestin Signaling Sustains Organ Dysfunction in Coxsackievirus B3 Infection of Mice

Meike Kespohl¹, Carl Christoph Goetzke¹, Nadine Althof, Clara Bredow, Nicolas Kelm¹, Sandra Pinkert, Thomas Bukur¹, Valesca Bukur, Kristin Grunz, Dilraj Kaur, Arnd Heuser, Michael Mülleder¹, Martina Sauter¹, Karin Klingel¹, Hartmut Weiler, Nikolaus Berndt¹, Matthias M. Gaida¹, Wolfram Ruf¹, Antje Beling¹

BACKGROUND: Accumulating evidence implicates the activation of G-protein-coupled PARs (protease-activated receptors) by coagulation proteases in the regulation of innate immune responses.

METHODS: Using mouse models with genetic alterations of the PAR2 signaling platform, we have explored contributions of PAR2 signaling to infection with coxsackievirus B3, a single-stranded RNA virus provoking multiorgan tissue damage, including the heart.

RESULTS: We show that PAR2 activation sustains correlates of severe morbidity—hemodynamic compromise, aggravated hypothermia, and hypoglycemia—despite intact control of the virus. Following acute viral liver injury, canonical PAR2 signaling impairs the restoration process associated with exaggerated type I IFN (interferon) signatures in response to viral RNA recognition. Metabolic profiling in combination with proteomics of liver tissue shows PAR2-dependent reprogramming of liver metabolism, increased lipid droplet storage, and gluconeogenesis. PAR2-sustained hypodynamic compromise, reprogramming of liver metabolism, as well as imbalanced IFN responses are prevented in β -arrestin coupling-deficient PAR2 C-terminal phosphorylation mutant mice. Thus, wiring between upstream proteases and immune-metabolic responses results from biased PAR2 signaling mediated by intracellular recruitment of β -arrestin. Importantly, blockade of the TF (tissue factor)-FVIIa (coagulation factor VIIa) complex capable of PAR2 proteolysis with the NAPc2 (nematode anticoagulant protein c2) mitigated virus-triggered pathology, recapitulating effects seen in protease cleavage-resistant PAR2 mice.

CONCLUSIONS: These data provide insights into a TF-FVIIa signaling axis through PAR2- β -arrestin coupling that is a regulator of inflammation-triggered tissue repair and hemodynamic compromise in coxsackievirus B3 infection and can potentially be targeted with selective coagulation inhibitors.

GRAPHIC ABSTRACT: A [graphic abstract](#) is available for this article.

Key Words: heart failure ■ infections ■ inflammation ■ myocarditis ■ proteomics

The coagulation system is a major defense pathway that cooperates with innate immune sensors to limit the spread of infections and supports immunity during restoration of tissue integrity after injury. TF (tissue factor), which serves as the receptor and catalytic cofactor for FVIIa (coagulation factor VIIa) in the initiation

of coagulation, shows structural similarities to cytokine receptors. In healthy tissue, TF expression is confined to subendothelial cells, and, upon traumatic injury, the receptor comes into contact with circulating coagulation proteases of the blood stream. The TF-FVIIa complex binds and activates coagulation zymogen FX, forming the

Correspondence to: Prof Wolfram Ruf, Center for Thrombosis and Hemostasis, Universitätsmedizin der Johannes-Gutenberg-Universität, Langenbeckstraße 1, 55131 Mainz, Germany, Email ruf@uni-mainz.de; or Prof Antje Beling, Institute of Biochemistry, Charité-Universitätsmedizin Berlin, Charitéplatz 1, 10117 Berlin, Germany, Email antje.beling@charite.de

Supplemental Material is available at <https://www.ahajournals.org/doi/suppl/10.1161/ATVBAHA.123.320157>.

For Sources of Funding and Disclosures, see page 863.

© 2024 The Authors. *Arteriosclerosis, Thrombosis, and Vascular Biology* is published on behalf of the American Heart Association, Inc., by Wolters Kluwer Health, Inc. This is an open access article under the terms of the [Creative Commons Attribution Non-Commercial-NoDerivs](#) License, which permits use, distribution, and reproduction in any medium, provided that the original work is properly cited, the use is noncommercial, and no modifications or adaptations are made.

Arterioscler Thromb Vasc Biol is available at www.ahajournals.org/journal/atvb

Nonstandard Abbreviations and Acronyms

| | |
|--------------------------------|--|
| AMPK | AMP-activated protein kinase |
| ASAT | aspartate aminotransferase |
| CVB3 | coxsackievirus B3 |
| FA | fatty acid |
| EPCR | endothelial cell protein C receptor |
| ERK1/2 | extracellular signal-regulated kinases 1 and 2 |
| FVIIa | coagulation factor VIIa |
| FXa | coagulation factor Xa |
| GO | gene ontology |
| GPCR | G-protein-coupled receptor |
| IFN | interferon |
| IL | interleukin |
| IRF3 | interferon regulatory factor-3 |
| ISG | interferon-stimulated gene |
| ISG15 | interferon-stimulated gene of 15 kDa |
| LD | lipid droplet |
| LDH | lactate dehydrogenase |
| LV | left ventricle |
| MyD88 | myeloid differentiation primary response 88 |
| NAPc2 | nematode anticoagulant protein C2 |
| NF-κB | nuclear factor kappa B |
| PAR | protease-activated receptor |
| PCR | polymerase chain reaction |
| PKC | protein kinase C |
| TF | tissue factor |
| TLR | toll-like receptor |
| TNF-α | tumor necrosis factor-alpha |
| TRIF | toll/interleukin-1 receptor domain-containing adapter-inducing interferon-beta |
| WT | wild type |

ternary TF-FVIIa-FXa (coagulation factor Xa) complex and following release of FXa triggers coagulation and thrombosis. Notably, inflammation and oxidative stress trigger TF expression, also in vascular endothelial cells,¹ hepatocytes,² cardiomyocytes, and innate immune cells,^{3,4} and thereby expand the receptor repertoire for coagulation proteases to sites of inflammation. Beyond initiation of clotting, TF complexed with coagulation proteases FVIIa and FXa functions as a hormone-like signaling molecule that regulates vital processes in infection. TF in complex with FVIIa or FVIIa-FXa protease supports proteolytic cascades that mediate downstream signaling by the PAR (protease-activated receptor) family. PARs are GPCRs (G-protein-coupled receptors) and, among many activating proteases, signaling is induced by coagulation proteases, each showing cleavage selectivity by unique

Highlights

- TF (tissue factor)-FVIIa (coagulation factor VIIa) signaling axis through PAR2 (protease activated receptor 2)- β -arrestin coupling is a regulator of inflammation-triggered tissue repair and hemodynamic compromise.
- PAR2 activation sustains correlates of severe morbidity in coxsackievirus B3 infection.
- PAR2-dependent reprogramming of liver metabolism with increased lipid droplet storage and gluconeogenesis in coxsackievirus B3 infection.
- Canonical PAR2 signaling impairs the restoration process associated with exaggerated type I IFN (interferon) signatures.

interactions with the PAR's extracellular N-terminal domains. Proteolysis unmask a new N terminus that serves as a tethered ligand to activate canonical PAR2 G-protein signaling and RAS (rat sarcoma virus)-RAF (rapidly accelerated fibrosarcoma)-MEK (mitogen-activated protein kinase kinase)-dependent ERK1/2 (extracellular signal-regulated kinases 1 and 2) activation. Engaged with TF, FVIIa and FXa predominantly signal via PAR2. TF-bound coagulation proteases, FVIIa in the binary and TF-FVIIa-FXa in the ternary complex, form distinct signaling complexes with integrins⁵ or coagulation protease binding immune-related receptors,^{6,7} respectively, to exert unique downstream signaling.

Expanding evidence documents that TF/PAR2 signaling in infection regulates pathways that can influence the pathogen burden. For example, TF can be randomly incorporated into the envelope of Herpes simplex viruses, which promotes PAR2-dependent infection of the endothelium.⁸ In a primate Ebola virus infection model, blockade of TF markedly reduces the viral load, attenuates inflammation, and improves survival.⁹ The cellular signaling events that are provoked by TF-coagulation protease-PAR2 cleavage in infection can converge with TLR (toll-like receptor) signaling, as exemplified by PAR2-mediated enhancement of TLR4-MyD88 (myeloid differentiation primary response 88) signaling in the epithelial cell.^{10,11} On the contrary, PAR2 also has anti-inflammatory effects in myeloid cells.¹² Similarly, PAR2 activation can assist TLR3-mediated NF- κ B (nuclear factor kappa B) activation in epithelial cells, whereas PAR2 stimulation interferes with TLR3-dependent IRF3 (IFN regulatory factor-3) phosphorylation and IFN (interferon)- β expression.¹⁰

In the last 2 decades, the physiological significance of the cross talk between coagulation and immunity came into focus for infection with coxsackievirus B3 (CVB3), a nonenveloped single-stranded (+) RNA enterovirus from the family of Picornaviridae. Enterovirus disease has medical impact, with newborn infants and young children being at risk for septic-like disease, particularly

during periods of high enterovirus prevalence. CVB3-associated health problems, such as pancreatic failure, cardiovascular collapse, and hepatitis, can be studied in mice.^{13,14} Mouse CVB3 infection models showed that the innate immune system senses CVB3 infection by recognizing viral components, such as double-stranded RNA by TLR3, and thereby triggers potent antiviral responses. Engagement of the endosomal TLR3 with its respective ligands stimulates the adaptor molecule TRIF (toll/interleukin-1 receptor domain-containing adapter-inducing interferon-beta) and propagates the production of type I IFNs. In fact, CVB3 infection studies demonstrated the antiviral properties of each component of the TLR3-TRIF-IFN pathway,^{15–17} and some supportive evidence for the clinical implications of TLR3 signaling has been seen in patients.¹⁸ IFN production and the cellular responses triggered by IFN signaling were uniformly defined as requirements for virus control, survival, and the proper induction of tissue repair.^{19–23} IFNAR (interferon-alpha/beta-receptor) signaling, activated in CVB3-infected liver tissue, ameliorates liver injury²³ and controls liver metabolism via its downstream effector molecule ISG15 (IFN-stimulated gene of 15 kDa).²⁴ Notably, the TLR adaptor molecule MyD88, known to interfere with the TLR3-TRIF-IRF3 axis,²⁵ impacts on TRIF-IRF3-controlled IFN production in CVB3 infection and promotes virus replication in mouse hearts.²⁶ Importantly, MyD88 stimulates inflammatory responses and promotes death in mouse CVB3 infection models,²⁶ and these effects are, at least partially, attributed to TLR4 signaling.²⁷

Our current understanding of how the coagulation system regulates innate immune responses and how such cross talk controls tissue repair in CVB3 infection is based on a mouse myocarditis model with lost PAR signaling platforms.^{28,29} PAR2 deletion coincided with less viral burden and mitigated cytotoxicity in the heart,²⁹ whereas PAR1 deficiency showed the opposite effect, with elevated viral cytotoxicity.²⁸ Notably, different PARs couple to overlapping and distinct sets of signaling pathways and might regulate cell physiology differentially.³ A loss of the PAR2 signaling platform may be complicated by deregulated signaling of other PAR family members,^{30,31} and this points to limitations of PAR knockouts in defining PAR-specific biological processes. Here, we investigated canonical PAR2 signaling by coagulation proteases and defined the role of cellular β -arrestin recruitment downstream of PAR2 activation in CVB3 infection. We uncovered a signaling pathway that sustains CVB3-triggered organ dysfunction and controls tissue repair.

MATERIALS AND METHODS

Please see the Major Resources Table in the [Supplemental Material](#). All supporting data are available within the article (and its [Supplemental Material](#)). The mass spectrometry proteomics

data have been deposited to the ProteomeXchange Consortium via the PRIDE (Proteomics Identification Database)³² partner repository with the data set identifier PXD042272.

Mice

Wild-type (WT) controls (PAR2^{fl/fl}) on the C57BL/6(N) background (4–6 weeks old) were used as WT controls to exclude potential differences introduced by the targeting strategy. Mice were injected intraperitoneally with 10⁵ PFU (plaque-forming units) CVB3 Nancy (CVB3[N])³³ or H3 (CVB3[H]), routinely in the morning around 11 am. CVB3(H) was generated using the pBKCMV-H3 plasmid (kindly provided by Andreas Henke, Institute of Virology and Antiviral Therapy, Jena University Hospital, Friedrich Schiller University, Jena, Germany).³⁴ Sex is a highly relevant factor for antiviral immunity, including IFN responses. Male mice were chosen for all experiments, which generally avoids attenuating effects observed in females. Moreover, sex has not been specifically addressed in prior studies on PAR2 contributions in viral pathogenesis.²⁹ In C57BL/6(N) mice, PAR2 was rendered cleavage insensitive to all proteases (R38E) or FXa selectively (G37I) by knock-in mouse technology that introduced site-specific mutations.^{35,36} PAR2- β -arrestin coupling-deficient mice are based on findings shown by DeFea et al,³⁷ and the generation is shown here.³⁸ PKC (protein kinase C) phosphorylation sites S365 and T368 in the PAR2 C-terminal intracellular domain were mutated to A (PAR2 S365T368/A). All mouse strains were generated with ES (embryonic stem) cells or oocytes from C57BL/6 N mice, and experiments were performed on this background. PAR2 R38E and PAR2 G37I mice were generated with the same targeting strategy as PAR2^{fl/fl} mice, which were used as WT controls. All mutant strains were transferred from Johannes Gutenberg University Medical Center Mainz to the animal facilities of Charité–Universitätsmedizin Berlin for further breeding. For NAPc2 (nematode anticoagulant protein c2) studies, in addition to WT controls (PAR2^{fl/fl} on C57BL/6[N]), male A/J mice (7–8 weeks) were purchased from Envigo and infected with 1×10⁴ pfu of CVB3(N). Clinical inspection was performed at least daily, and mice were scored for these parameters: body weight, activity, behavioral changes, movement. A drop of the body weight >25% resulted in euthanization of mice. On the final day of each infection study, after echocardiography, organs were collected for further analysis and immediately frozen in liquid nitrogen. Sample collection took place between 8 and 11 AM. There was no starvation period before euthanizing the animals. Organs were stored at –80 °C. Retrobulbar blood sampling was performed for all CVB3(H) infection studies and experiments investigating the effects of NAPc2. Blood glucose levels were determined using an Accu-Chek glucometer (Roche Diabetes Care, Indianapolis, IN, USA). For the determination of wet-dry tissue weight ratio, lungs were removed and were weighed, dried for at least 48 hours at room temperature, and reweighed. This study was performed in accordance with the recommendations in the Guide for the Care and Use of Laboratory Animals of the German Animal Welfare Act, which is based on the directive of the European Parliament and the Council of Europe Convention for the Protection of Vertebrate Animals Used for Experimental and Other Scientific Purposes (ETS123). This study was approved by the local authorities for animal welfare in Berlin (permit number: G0064/16). All efforts were made to minimize suffering.

TF Inhibitor

Recombinant NAPc2 was obtained from Corvas International, Inc.³⁹ Starting on the day of infection, mice received a daily intraperitoneal injection of 1 mg/kg NAPc2 in PBS.

Echocardiography

For echocardiography, mice were anesthetized with 1.5% to 2% isoflurane and kept warm on a heated platform. Temperature and ECG were monitored continuously during the exam. Cardiac function and morphology were assessed with a VisualSonics Vevo 770 or 3100 High-Frequency Imaging System using a high-resolution transducer. Standard imaging planes, M-mode, and functional calculations were obtained. For the parasternal long-axis left ventricular (LV) trace, the average systolic or diastolic volume in B mode is based on the rotational volume of the LV trace at systole or diastole around the long axis of the spine. The parasternal long-axis view of the LV was used to guide calculations of ventricular dimensions (M mode), volumes (B mode; LV vol; d=LV trace end diastolic; LV vol; s=LV trace end systolic; stroke volume using the formula $SV=LV\ vol;d-LV\ vol;s$), and LV ejection fraction (B mode using the formula $LVEF=100\times[LV\ vol;s-LV\ vol;d]/[LV\ vol;d]$). Images in short-axis view were acquired at the midpapillary level of the LV for calculation of fractional area shortening (%fractional area change, B mode) using the formula $FAC=100(\text{end-diastolic area}-\text{end-systolic area})/(\text{end-diastolic area})$. Myocardial performance index (Tei index) $=(\text{isovolumic contraction time}+\text{isovolumic relaxation time})/\text{ejection time}$. Myocardial performance index is a Doppler index of combined systolic and diastolic myocardial performance myocardial systolic dysfunction. M-mode echocardiographic images were recorded at the level of the papillary muscles from the parasternal short-axis view. All measurements were performed by the Animal Phenotyping Platform of the Max-Delbrück-Center for Molecular Medicine in Berlin.

Serum Analysis

Serum was obtained by centrifugation of whole blood at 10 000 rcf (relative centrifugal force) for 15 minutes and was stored at -80°C . Serum activities of liver enzymes were determined by an external veterinary diagnostic laboratory (SYNLAB Vet, Berlin, Germany). Glucose concentration was determined using an Accu-Chek glucometer (Roche). Bead-based BioPlex Pro Mouse Cytokine Assay and Chemokine Assay (BioRad, Hercules, CA) were used to determine the levels of TNF- α (tumor necrosis factor-alpha), IL (interleukin)-6, IL-10, IFN- γ , CCL2, CCL3, and CCL5.

Histology

Tissue samples were fixed in HistoFix (1 \times PBS, 4% ROTI-Histofix), embedded in paraffin, and stained with hematoxylin and eosin. To quantify myocardial damage comprising cardiac cell necrosis, inflammation, and scarring, a transverse cardiac section obtained from the area below the atrioventricular valves was analyzed at 100-fold to 200-fold magnification and a myocarditis score from 0 to 4 was applied (0: no inflammatory infiltrates, 1: small foci of inflammatory cells between myocytes, 2: larger foci of >100 inflammatory cells, 3: $\leq 10\%$ of cross-section involved, 4: 10%–30% of a cross-section involved). The size of the liver tissue probes was ≈ 0.5 to 1 cm and covered

representative amounts of the whole organ. For evaluation, we examined at least 5 representative high-power fields using a light microscope (Olympus BX51; Olympus Germany, Hamburg, Germany). The field area of the used microscope in the 40 \times objective is 0.24 mm². Liver pathology was categorized on sections of the left lobe based on the severity of inflammation and necrosis using a scoring system adapted from Veteläinen et al⁴⁰: 0: no inflammation/necrosis, 1: scattered immune cells/mild necrosis ($<10\%$), 2: immune cell foci/marked necrosis (10%–50%), and 3: diffuse immune cell infiltrates/severe necrosis ($>50\%$). The score in uninfected mice was zero. For visualization of perilipin2, liver samples were stained using an anti-ADFP (adipocyte differentiation related protein) antibody (PA5-79830; Thermo Fisher Scientific, Waltham, MA). Tissue sections were scored semiquantitatively ($\times 40$ magnification in at least 5 fields) and the staining distribution and intensity were graded according to the criteria listed Table 1.⁴¹

Isolation of Immune Cells From Mouse Tissue

Splenocytes were isolated according to standard procedures, as outlined in the study by Althof et al.⁴² After excision, the heart was flushed with 15 mL PBS. An amount of heart tissue defined by weight was minced in RPMI (Roswell Park Memorial Institute) 1640 medium (Gibco, Thermo Fisher Scientific) containing 10% (v/v) fetal calf serum (Sigma, Thermo Fisher Scientific), 1% (v/v) penicillin/streptomycin (Gibco), 30 mmol/L HEPES, 0.1% (w/v) collagenase type 2 (Worthington Biochem, Lakewood, NJ) and 0.015% (w/v) DNase I (Sigma). Tissue digestion was performed by incubating at 37 $^{\circ}\text{C}$ for 30 minutes while shaking at 800 rpm. EDTA was added at a final concentration of 10 mmol/L before washing with PBS. Cells were subsequently passed through a 70- μm cell strainer (BD Biosciences, Franklin Lakes, NJ), recovered by centrifugation (10 minutes, 480 rcf), and resuspended in fluorescence-activated cell sorting (FACS) buffer. Samples were chilled on ice until flow cytometry was performed.

Flow Cytometry

Equal numbers of splenocytes or cells purified from 20 mg heart tissue were incubated (20 minutes at 4 $^{\circ}\text{C}$) in FACS buffer (1 \times PBS, 2% fetal calf serum, 2 mmol/L EDTA) containing an anti-mouse Fc receptor blocking reagent (1:50; Miltenyi Biotec, Mönchengladbach, Germany). Afterward, fluorochrome-conjugated antibodies were added and incubated for 20 minutes at 4 $^{\circ}\text{C}$ in the dark: CD8-PB (clone 53-6.7), MHC (major histocompatibility class) II-A[b]-FITC (clone AF6-120.1), CD3-BUV737 (clone 145-2C11), B220-BUV395 (clone R43-6B2), and NK1.1-PE (clone Pk136) were purchased from BD

Table 1. Histological Grading Scores for Perilipin 2

| Percentage of IHC positive cells | Intensity of staining | Multiplication score |
|----------------------------------|-----------------------|--|
| 1: 0%–5% | 0: negative | 0 or 1: negative expression |
| 2: 5.1%–50% | 1: weak | 2–4: weakly positive expression |
| 3: 50.1%–80% | 2: moderate | 5–8 (++) : positive expression |
| 4: 80.1%–100% | 3: intense | 9–12 (+++) : intensively positive expression |

IHC indicates immunohistochemistry.

Biosciences and F4/80-APC (clone BM8), CD11b-BV510 (clone M1/70), Ly6G-BV605 (clone 1A8), CD11c-PE/Dazzle (clone N418), Ly6C-PE-Cy7 (clone HK1.4), CD4-PerCP-Cy5.5 (clone RM4-5), and CD45.2-BV711 (clone 104) from Biolegend (San Diego, CA). For the analysis of immune cell populations in A/J mice, MHCII I-A[b] and NK1.1 were replaced by CD49b-PE (clone DX5) and MHCII I-A[k] (clone 10-3.6), respectively. The antibodies used for surface staining of splenocytes were the following: CD4-V500 (clone RM4-5), CD8-PB (clone 53-6.7), CD3-BUV737 (clone 145-2C11), CD69-APC (clone H1.2F3), CD44-BV650 (clone IM7), and CD45.2-BV711 (clone 104) from Biolegend. After 2 wash steps with FACS buffer (centrifugation: 3 minutes at 420 rcf), cells were resuspended in 150 μ L of the fixable viability dye eFluor 780 (Invitrogen, Thermo Fisher Scientific), diluted 1:1000 in PBS and incubated for 30 minutes on ice protected from light. After serial wash steps with PBS followed by fixation in FACSFix (1 \times PBS, 2% ROTI Histofix; Carl Roth, Karlsruhe, Germany), cells were acquired on a FACS Symphony flow cytometer (BD Biosciences). Data were analyzed using the FlowJo v10.6 software (BD Biosciences). To quantify total cell numbers in heart tissue, 123count eBeads (Invitrogen) were used according to the manufacturer's protocol. Reported numbers were normalized for the utilized tissue weight, yielding the number of cells per milligram of tissue. For heart tissue, the following cell subsets were defined based on the gating procedure shown by Pinkert et al⁴³: macrophages: CD45⁺ CD11b⁺ B220⁻ CD3⁻ NK1.1⁻ Ly6G[1]CD11c^{+/-} F4/80⁺, inflammatory monocytes: CD45⁺ CD11b⁺ B220⁻ CD3⁻ NK1.1⁻ Ly6G⁻ CD11c⁻ F4/80⁻ Ly6C^{hi}, stationary monocytes: CD45⁺ CD11b⁺ B220⁻ CD3⁻ NK1.1⁻ Ly6G⁻ CD11c⁻ F4/80⁻ Ly6C^{low}, neutrophils: CD45⁺ CD11b⁺ B220⁻ CD3⁻ NK1.1⁻ Ly6G⁺ SSC^{hi}, dendritic cells: CD45⁺ CD11b⁺ B220⁻ CD3⁻ NK1.1⁻ Ly6G⁻ CD11c⁺ F4/80⁻ MHCII⁺, B cells: CD45⁺ CD11b⁻ B220⁺ CD3⁻, T cells: CD45⁺ CD11b⁻ B220⁻ CD3⁺.

Quantitative Real-Time Polymerase Chain Reaction and Polymerase Chain Reaction Array Analysis

RNA was isolated using the TRIzol (Ambion; Thermo Fisher Scientific) method according to the manufacturer's instructions. Remaining DNA was removed by digestion with DNase I (Invitrogen) at 37 °C for 15 minutes followed by enzyme deactivation at 65 °C for 10 minutes. RNA of 250 to 1000 ng was reverse transcribed with MLV Reverse Transcriptase (Promega, Madison, WI) in combination with random hexamer primers (Roche, Basel, Switzerland). TaqMan polymerase chain reaction (PCR) was performed using primers and probes of TaqMan gene expression assays (Life Technologies) and the following combinations of primers and probes: *HPRT* (hypoxanthin-guanin-phosphoribosyltransferase) forward: 5'-ATC ATT ATG CCG AGG ATT TGG AA-3', reverse: 5'-TTG AGC ACA CAG AGG GCC A-3', probe: 5'-FAM-TGG ACA GGA CTG AAA GAC TTG CTC GAG ATG-3'TAMRA; *CVB3* forward: 5'-CCC TGA ATG CGG CTA ATC C-3', reverse: 5'-ATT GTC ACC ATA AGC AGC CA-3', probe: 5'-FAM-TGC AGC GGA ACC G-MGB3'. Quantitative real-time PCR was conducted on a StepOnePlus real-time PCR system. TaqMan assays for *HPRT* served as endogenous controls and were used to calculate relative expression using the Δ Ct method. Type I IFN-related gene

expression was quantified using mouse type I IFN response QuantiNova LNA PCR Focus Panel (SBMM-016Z; Qiagen, Venlo, NL). RNA of 2000 ng was subjected to cDNA synthesis reaction using QuantiNova Reverse Transcription Kit (Qiagen). According to the manufacturer's instructions, cDNA was mixed with the components of QuantiNova SYBR Green RT-PCR Kit (Qiagen) and dispensed into each well of the PCR array, which was conducted on a StepOnePlus real-time PCR system (Thermo Fisher Scientific). Downstream analysis steps were computed by R.⁴⁴ Using a library for the analysis of high-throughput quantitative real-time PCR data,⁴⁵ we calculated standard Δ Ct values. For this, we subtracted the mean of the following controls from all other Ct values: *Actb*, *Gapdh*, *Gusb*, and *Hsp90ab1*. *Actb*, *Gapdh*, *Gusb*, *Hsp90ab1*, *B2m*, *MGDC*, *PPC*, and *QIC* served as internal controls and are not shown in the figures. We used the package *limma*⁴⁶ for pairwise comparison of all groups ($\Delta\Delta$ Ct values) with the function *limmaCtData* setting *stringent=FALSE* and *spacing=1*.

Quantification of Infectious Viral Particles

Plaque assays were performed on subconfluent monolayers of GMK (green monkey kidney) cells for CVB3(N) and HeLa (Henrietta Lacks) cells for CVB3(H). Cells were incubated with serial 10-fold dilutions of supernatant from homogenized mouse tissue. Plaque assays on GMK cells were performed as described previously.²⁴ CVB3(H)-infected samples were applied to HeLa cells for 30 minutes at 37 °C, before supernatants were removed and monolayers were overlaid with 0.7% agarose (Serva) containing Eagle minimal essential medium and 9.2% fetal calf serum. Two days later, cells were stained with 0.5% MTT-PBS (3-[4,5-dimethylthiazol-2-yl]-2,5-diphenyltetrazolium bromide; Sigma).

Sample Preparation for Proteomics

Protein was extracted from 5 mg of mouse liver and DNA sheared in 75 μ L of lysis buffer (1% SDS, 0.1 mol/L ABC [ammoniumbicarbonat], 1.25 \times PIC [protease inhibitor cocktail]) in AFA-TUBE TPX Strips on Covaris LE220Rsc by focused ultrasonication (PIP [peak incident power] 450 W, DF [duty factor] 25%, CPB [cycles per burst] 200, 2 repeats, 300 s pulse, 20° C). Samples were cleared from debris (2500g for 5 minutes) and proteins quantified (Pierce BCA, 23225; Thermo Fisher Scientific). SP3 (solidphase-enhanced sample-preparation) protein preparation used 100 μ g total protein using a Biomek i7 workstation with single-step reduction and alkylation.⁴⁷ Briefly, 16.6 μ L reduction and alkylation buffer (40 mmol/L TCEP [tris(2-carboxyethyl) phosphine], 160 mmol/L CAA [2-chloroacetamide], 200 mM ABC) were added, samples incubated for 5 minutes at 95 °C, and cooled to room temperature. Proteins were bound to 500 μ g paramagnetic beads (1:1 ratio of hydrophilic/hydrophobic beads) by adding acetonitrile to 50%. Samples were washed twice with 80% ethanol and once with 100% acetonitrile, before reconstitution in 35 μ L 100 mmol/L ABC. Digestion was completed overnight at 37 °C using a trypsin/LysC enzyme mix (Promega) at a ratio of protein:enzyme of 50:1 (w/w) and stopped with formic acid (0.1%). The peptides were stored at -80 °C until analysis by LC-MS (liquid chromatography-tandem mass spectrometry) without further conditioning or cleanup.

Proteome Analysis by DIA LC-MS and DIA-NN

A trap column (PepMap C18, 5 mm×300 μm×5 μm; 100 Å; Thermo Fisher Scientific) was used to concentrate 1.25 μg tryptic peptides, using buffer containing 2:98 (v/v) acetonitrile/water containing 0.1% (v/v) trifluoroacetic acid, flow rate of 20 μL/minute, and separated on a 500-mm analytical LC column (Acclaim PepMap C18, 2 μm; 100 Å; 75 μm; Thermo Fisher Scientific). The mobile phase was 0.1% (v/v) formic acid in water (solvent A) and 80% acetonitrile in 0.1% (v/v) formic acid (solvent B). During the 115-minute total acquisition time, the solvent B was gradually increased over the course of 90 minutes from 8% to 45% at a flow rate of 250 nL/min. Q-Exactive Plus Orbitrap operated in centroid mode with 12 m/z DIA (data-independent acquisition) spectra (12 m/z precursor isolation windows at 17 500 resolution; AGC (automatic gain control) target, 1e6; maximum inject time, 60 ms; 27 NCE [normalized collision energy]) using an overlapping window pattern. Precursor MS spectra (m/z 400–1000) were analyzed at 35 000 resolution after 60-ms accumulation of ions to a 1e6 target value in centroid mode. Raw data were processed using DIA-NN (neural network) 1.8⁴⁸ with scan window size set to 11 and MS2 and MS1 mass accuracies set to 20 and 10 ppm, respectively. A spectral library free approach and mouse UniProt (UP000000589, reviewed, canonical, downloaded on January 27, 2021)⁴⁹ were used for annotation. The output was filtered at 1% FDR (false discovery rate) on peptide level.

Proteome Data Analysis

Further data analysis was performed with the Perseus software (version 1.6.2.1) after loading the protein groups table provided by DIA-NN of liver proteomes. Hits identified in the reverse database and as potential contaminants were removed, and protein label-free quantification intensities for each sample were log₂ transformed. Replicate samples were grouped, proteins with <3 valid values in at least 1 group were removed, and missing values were imputed from a normal distribution around the detection limit. To identify proteins that were significantly regulated across all samples, groups were defined based on genotypes and time after infection, and a 2-way ANOVA test was performed to compare the protein intensities in the infection group with the genotype group (Table S1 [WT+R38E] and Table S3 [WT+S365T368/A], respectively). The intensities of significantly regulated proteins are shown in the heatmap in Figure 4A (WT+R38E) and Figure S5 (WT+S365T368/A) after Z scoring and nonsupervised hierarchical clustering. To further dissect the regulation between WT and R38E or WT and S365T368/A mice, gene ontology (GO) enrichment analysis (Table S2 [WT+R38E] and Table S4 [WT+S365T368/A], respectively) was performed on the protein lists derived from the heatmap. GO term enrichment analysis was performed using the GO consortium bioinformatics resources.^{50–52}

Computational Simulation of Liver Metabolism in Infection

Hepatokin1—a model of central liver metabolism⁵³—was used to simulate the metabolic alterations during viral infection in dependence of the PAR2 activity. We constructed strain- and condition-dependent metabolic models, calculating the maximal activity for each enzyme and transporter in the model

according to the label-free quantification intensities obtained from DIA-NN analysis. We simulated the hepatic exchange flux for the indicated substrates/metabolic processes. For each condition, experimentally determined blood glucose levels as depicted here, as well as reference values for serum free fatty acids (FAs) obtained from CVB3-infected WT mice²⁴ were used as model input to calculate corresponding exchange fluxes.

Statistics

Statistical analysis of the data was performed in GraphPad Prism v7.00 and v8.00 for Windows (GraphPad Software, La Jolla, CA). Data are plotted as individual points. Data were first tested for normal distribution using the D'Agostino–Pearson test. If not indicated otherwise, data summary is given as mean±SEM. Logarithmic data (virus titer, semiquantitative RNA quantification) measured on a linear scale were transformed logarithmically before data plotting and analysis. Unpaired *t* tests were used for 2-group comparisons of normally distributed data. If samples had unequal variances (determined by an *F* test), an unpaired *t* test with the Welch correction was used. For multiple-group comparison, 2-way ANOVA tests were used, with repeated measures in Figures 1B and 2E and using a paired 2-way ANOVA test in Figure 1C and 1D, all followed by either a Tukey or a Sidak multiple comparison test as specified in the figure or table legends. Survival rates were compared using a log-rank (Mantel-Cox) test. The significance threshold for all tests was set at the 0.05 level.

RESULTS

PAR2 Exacerbates CVB3-Triggered Pathology Independent of FXa-Dependent PAR2 Signaling

Mouse models with site-specific mutations in the *F2r1* gene, rendering PAR2 cleavage resistant to proteases (R38E),^{35,36} were used to study canonical protease-dependent cell signaling in CVB3 infection. To dissect whether FXa, which affects CVB3 infection by as yet unknown mechanisms,⁵⁴ controls PAR2 signaling as well, we investigated PAR2 mutants that are selectively cleavage insensitive to FXa (PAR2-G37I; Figure 1A). CVB3(N) infection in WT mice provoked a systemic inflammatory response with loss of body mass (Figure 1B), as well as a drop in plasma glucose concentration (Figure 1C). The body mass gradually declined, starting 2 days after infection and plateauing after 6 days. PAR2-G37I mice showed the same phenotype as WT controls, whereas resistance to proteolytic PAR2 cleavage in PAR2-R38E mice resulted in higher body mass after 7 and 8 days with an accelerated return to baseline levels in comparison to both WT and PAR2-G37I mice (Figure 1B). Correspondingly and indicative for lower energy expenditure, PAR2-R38E mice showed no relevant reduction of blood glucose, whereas both PAR2-G37I and WT mice presented with a marked depression of blood glucose after 8 days (Figure 1C). Another systemic feature of CVB3 infection was hypothermia, which occurred similarly in PAR2-G37I and WT mice. PAR2-R38E mice showed

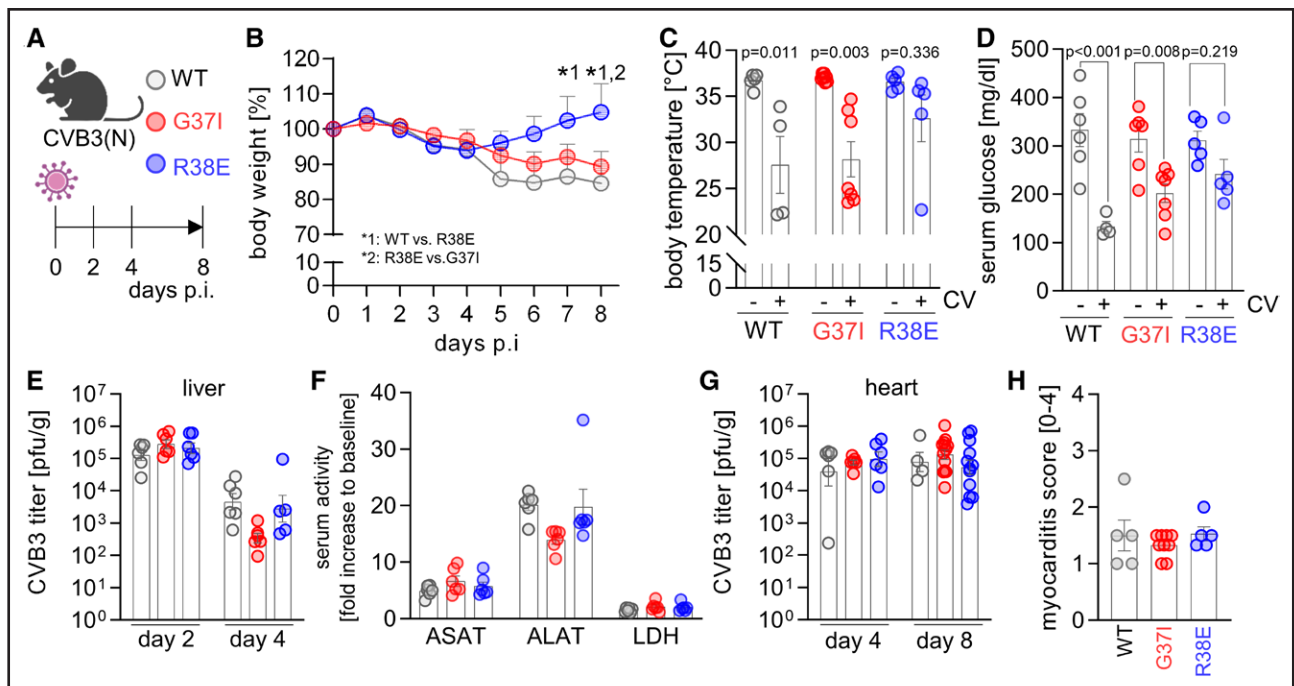


Figure 1. Canonical PAR2 (protease activated receptor 2) cleavage exacerbates coxsackievirus B3 (CVB3[N])-triggered pathology independent of Xa-dependent PAR2 proteolysis.

A, Male wild-type (WT), PAR2-G37I (G37I), and PAR2-R38E (R38E) mice were infected with CVB3(N). Mice were euthanized after 2, 4, or 8 days. **B**, Body weight changes after infection. Data as relative body weight of each animal, normalized to their weight on day 0 (WT, n=5; PAR2-G37I, n=7; PAR2-R38E, n=5). Repeated measures of 2-way ANOVA analysis followed by a Tukey multiple comparison *t* test with * indicating significant differences. **C**, Serum glucose levels were determined 8 days after infection (WT, n=4; PAR2-G37I, n=7; PAR2-R38E, n=5), as well as uninfected controls. **D**, Body temperature at baseline and 8 days after infection (WT, n=5; PAR2-G37I, n=7; PAR2-R38E, n=5). **C** and **D**, Paired 2-way ANOVA analysis followed by a Sidak multiple comparison *t* test. **E**, The number of infectious viral particles determined by plaque assay of liver tissue at the indicated time points (n=6). **F**, Relative quantification of serum activity for ASAT (aspartate aminotransferase), ALAT (alanine aminotransferase), and LDH (lactate dehydrogenase) after 2 days; values normalized to baseline (n=6). **G**, The number of infectious viral particles determined by plaque assay for heart tissue at the indicated time points (WT: n=6; PAR2-R38E: day 4, n=6; day 8, n=12). **H**, Scoring of cardiac sections stained with hematoxylin/eosin. Each dot represents a different animal (WT, n=5; PAR2-G37I, n=9; PAR2-R38E, n=5).

only a mild, insignificant drop of the body temperature (Figure 1D). From these results, we conclude that canonical PAR2 signaling, independent of proteolytic cleavage by FXa, converges with virus-triggered inflammatory responses.

To investigate how PAR2 signaling affects virus infection, we monitored virus titers after 2 and 4 days in liver, as well as after 4 and 8 days in the heart tissue. In the liver, the high virus concentration at day 2 markedly declined at day 4 after infection (Figure 1E). Notably, the viral cytotoxicity triggered by CVB3(N) infection induced a rather mild hepatic injury with ≈ 20 -fold increased serum ALAT activity after 2 days (Figure 1F), corresponding to the acute phase of CVB3 infection. As expected, virus titers in heart tissue remained at an elevated level for up to 8 days (Figure 1G). Neither PAR2-G37I nor PAR2-R38E mice showed alterations in viral titers in comparison to WT controls (Figure 1E and 1G; Figures S9A and S13A). This argues against a PAR2-directed control of virus elimination that might explain the enhanced pathogenic effects seen in WT mice in comparison to PAR2-R38E mice. We scored the extent of myocardial necrosis

and inflammation in heart tissue sections and found mild myocarditis after 8 days (Figure 1H), which represents the subacute phase of infection with peak inflammatory response in the heart (Figure S1A and S1B). We conclude that PAR2 signaling provokes a hypodynamic phase with hypoglycemia and hypothermia emerging despite unaltered virus control.

Canonical PAR2 Signaling Sustains Hemodynamic Compromise

Because CVB3(N) infection sustains a fairly mild cause of infection in C57BL/6 mice, we explored in more detail how PAR2 signaling influences CVB3-triggered pathology by infecting PAR2-R38E mice and WT controls with CVB3 H3 (CVB3[H]; Figure 2A). Infection of mice with CVB3(H) triggers myocarditis, but in contrast to CVB3(N), this strain also induces severe injury of liver tissue during the acute phase,²¹ and the mice develop a profound hypodynamic condition leading to hemodynamic compromise and death.²² In fact, the acute phase is characterized by a substantial drop of plasma

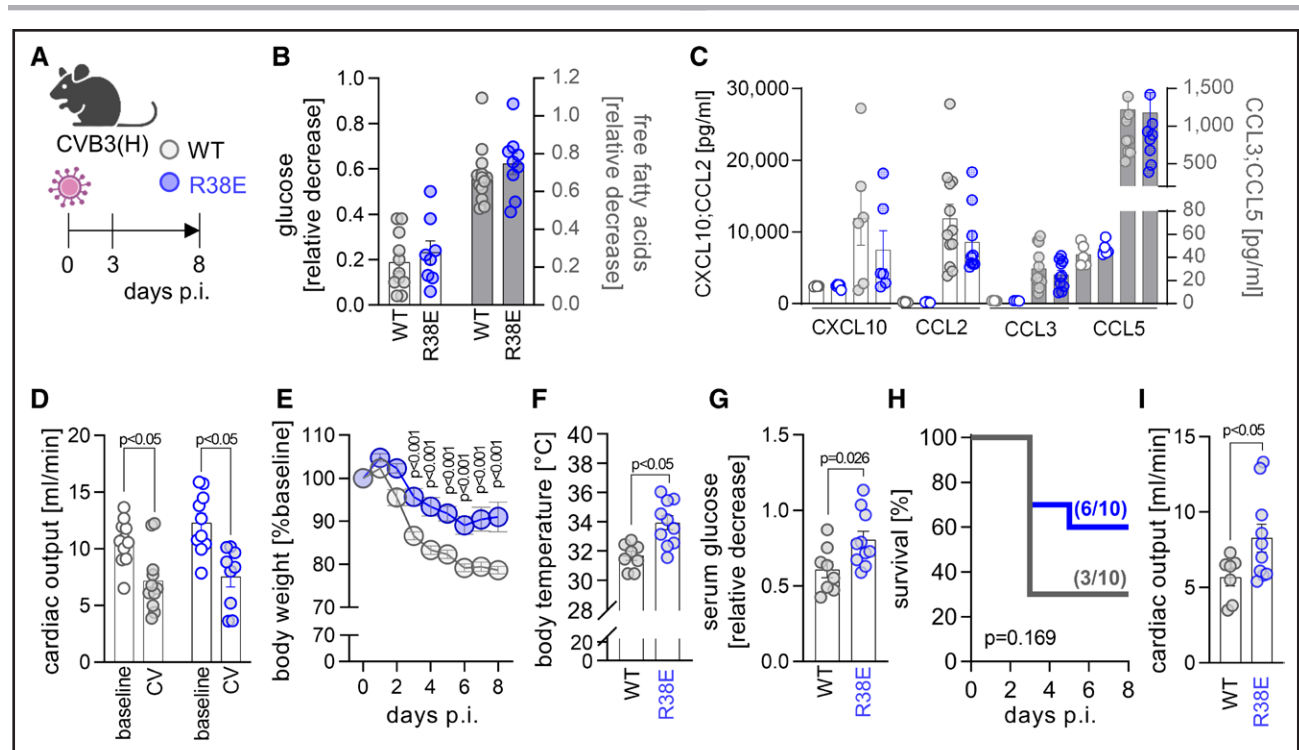


Figure 2. PAR2 (protease activated receptor 2) signaling results in hypodynamic compromise during coxsackievirus B3 (CVB3[H]) infection.

A, Protease cleavage-resistant male PAR2-R38E mice and wild-type (WT) controls were infected with CVB3(H). **B**, Serum concentration for glucose (blank columns; WT, n=11; PAR2-R38E, n=13) and free fatty acids (gray columns; WT, n=8; PAR2-R38E, n=9) after 3 days. The shown values were normalized to baseline controls. **C**, Multiplex chemokine profiling for CXCL10 (chemokine (C-X-C motif) ligand 10), CCL2 (chemokine (C-C motif) ligand), CCL3, and CCL5 of serum obtained from CVB3-infected WT and PAR2-R38E mice (day 3: shaded circles), as well as naive controls (blank circles; control: n=5 of each strain; day 3: WT, n=6–12; PAR2-R38E, n=6–10; varying for the different chemokines). **D**, Mice subjected to echocardiography with Vevo3100 (WT, n=11; PAR2-R38E, n=10) before and 3 days after CVB3 infection and calculation of the cardiac output. **E**, Shown values are the body weight change of each animal during infection, normalized to its initial body weight (WT, n=8; PAR2-R38E, n=10). Repeated measures of 2-way ANOVA analysis followed by a Tukey multiple comparison *t* test with * indicating significant differences. **F**, Body temperatures after 8 days (WT, n=8; PAR2-R38E, n=10). **G**, Serum glucose levels after 8 days normalized to baseline measurements (WT, n=8; PAR2-R38E, n=10). **H**, Survival monitored up to day 8. Survival curves were estimated from the Kaplan-Meier procedure with the log-rank (Mantel-Cox) test. **I**, Cardiac output calculated by echocardiography with Vevo3100 after 8 days (WT, n=7; PAR2-R38E, n=10).

nutrients, such as glucose and FAs (Figure 2B), together with signs of systemic inflammation, such as production of CXCL10 (chemokine (C-X-C motif) ligand), CCL2 (chemokine (C-C motif) ligand), CCL3, and CCL5 (Figure 2C). These parameters were not different 3 days after infection between WT and PAR2-R38E mice. The virus titer observed in the liver, pancreas, and heart tissue at this stage in CVB3(H) exceeded the titers in CVB3(N)-infected mice by several order of magnitude (Figures S2A and S9C). Despite this severe infection, the loss of PAR2 signaling in PAR2-R38E mice had no effect on viral control. The hypodynamic condition appeared to be overwhelming, and this phenotype was not substantially affected by PAR2 signaling after 3 days. The hypodynamic phase in CVB3 infection is determined by perturbation of cardiac output,^{42,55} and this has been shown to be unrelated to cardiac compromise, triggered by viral myocarditis.⁵⁶ We quantified cardiac performance by echocardiography and found a decreased cardiac output in CVB3(H)-infected mice after 3 days (Figure 2D).

Hypodynamic compromise was attributed to lower diastolic filling volume and bradycardia, without any evidence of a disturbance in systolic function. We found no effect of PAR2 inactivation on the cardiac output at this stage (Table 2).

As infection advanced to the subacute phase 8 days after infection, a deterioration in the hypodynamic condition of the mice due to PAR2 activation became evident. PAR2-R38E mice with cleavage-resistant PAR2 were markedly protected with a decrease in weight loss, higher body temperature, and blood glucose levels in comparison to WT controls (Figure 2E through 2G). Notably, the PAR2-promoted loss of body mass, characteristic of the manifestation of the catabolic phase in CVB3(H)-infected mice, was accelerated in comparison to CVB3(N) infection. Moreover, we observed a trend toward increased mortality attributable to PAR2 activation in CVB3(H) infection (Figure 2H). We quantified the cardiac output by echocardiography and documented a sustained reduction of

Table 2. Cardiac Output Impairment Triggered by CVB3 Infection

| | WT | | PAR2-R38E | |
|---------------------------------------|----------|-----------|-----------|-----------|
| | Control | Day 3 | Control | Day 3 |
| Heart rate, bpm | 467±16 | 363±17* | 503±19 | 388±21* |
| Trace EF, % | 55.1±2.4 | 55.9±3.9 | 59.3±2.2 | 62.1±4.9 |
| Cardiac output, mL/min | 10.6±0.6 | 7.2±0.8* | 12.3±0.9 | 7.5±0.9* |
| Stroke volume, μ L | 22.7±0.9 | 19.3±1.5 | 24.3±1.2 | 19.2±2.1 |
| Vol d, μ L | 41.0±1.8 | 35.7±3.0 | 41.4±2.4 | 31.2±2.5* |
| LVID-d, mm | 3.8±0.1 | 3.5±0.1 | 3.6±0.1 | 3.3±0.1 |
| LVID-s, mm | 2.7±0.1 | 2.5±0.2 | 2.5±0.1 | 2.2±0.2 |
| MV E, mm/s | 776±47 | 566±19* | 750±45 | 496±19* |
| MV _{decel} [†] , ms | 19.3±2.3 | 26.8±1.9* | 16.7±1.9 | 24.5±2.0 |
| IVRT, ms | 17.0±0.7 | 20.7±1.1 | 18.3±1.7 | 23.0±2.2 |

Mice were subjected to echocardiography (WT, n=11; PAR2-R38E, n=10; all males) before (control) and 3 d after CVB3 infection with CVB3(H; WT, n=11; PAR2-R38E, n=9; all males). Data are shown as mean values±SEM. Two-way ANOVA was performed, followed by a Tukey multiple comparison test to calculate *P* values, which are represented as

* when a significant difference ($P<0.05$) was found between baseline and day 3 measurements of the same mouse. Mitral valve E velocity was determined by pulse-wave Doppler at mitral valve. CVB3 indicates coxsackievirus B3; EF, ejection fraction; IVRT, isovolumic relaxation time; LVID-d, left ventricular internal diameter at diastole; LVID-s, left ventricular internal diameter at systole; MV_{decel}[†], mitral valve deceleration time; MV E, mitral valve E velocity; PAR2, protease-activated receptor 2; Vol d, volume at diastole; and WT, wild type.

the output in WT mice (Table 3). This was attributed to ongoing bradycardia, a hallmark of hypodynamic condition in mice, whereas the preload deficit, detected after 3 days, was no longer present at this stage. We evaluated the inflammatory response in viral myocarditis

Table 3. PAR2 Signaling Prolongs Hemodynamic Compromise

| | WT | | PAR2-R38E | |
|---------------------------------------|----------|-----------|-----------|------------|
| | Control | Day 8 | Control | Day 8 |
| Heart rate, bpm | 413±9 | 277±8* | 428±12 | 338±30* |
| Trace EF, % | 57.6±1.2 | 55.6±3.0 | 54.8±1.4 | 48.6±2.1 |
| Cardiac output, mL/min | 9.5±0.6 | 5.7±0.6* | 9.2±0.4 | 8.3±0.9 |
| Stroke volume, μ L | 22.8±1.2 | 20.4±1.8 | 21.4±0.8 | 24.2±0.9 |
| Vol d, μ L | 39.5±1.8 | 37.0±3.5 | 39.4±1.5 | 50.3±2.0*† |
| LVID-d, mm | 3.5±0.1 | 3.6±0.1 | 3.6±0.1 | 4.1±0.1*† |
| LVID-s, mm | 2.5±0.1 | 2.6±0.2 | 2.6±0.1 | 3.0±0.1*† |
| MV E, mm/s | 732±22 | 552±55*† | 705±18 | 712±47 |
| MV _{decel} [†] , ms | 23.6±1.3 | 39.6±4.2* | 21.9±1.5 | 30.9±2.9* |
| IVRT, ms | 20.5±0.4 | 34.7±2.4* | 19.2±0.6 | 28.0±2.7*† |

Mice were subjected to echocardiography (WT, n=23; PAR2-R38E, n=21; all males). WT (n=7) and PAR2-R38E (n=10; all males) were infected with CVB3(H). After 8 days, a second echocardiogram was obtained. Data are mean values±SEM. Two-way ANOVA was performed followed by a Tukey multiple comparison test. Mitral valve E velocity was determined by pulse-wave Doppler at mitral valve. CVB3 indicates coxsackievirus B3; EF, ejection fraction; IVRT, isovolumic relaxation time; LVID-d, left ventricular internal diameter at diastole; LVID-s, left ventricular internal diameter at systole; MV_{decel}[†], mitral valve deceleration time; MV E, mitral valve E velocity; PAR2, protease-activated receptor 2; Vol d, volume at diastole; and WT, wild type.

*Significant differences ($P<0.05$) between baseline and day 8 measurements.

†Significant differences ($P<0.05$) between WT and PAR2-R38E at day 8.

by flow cytometry-based enumeration of myeloid and lymphoid cells, as well as histology. This analysis did not uncover differences in the numbers of infiltrating immune cells between WT and PAR2-R38E mice. Myocardial tissue injury resulted in higher cardiac troponin T levels, but creatine kinase activity remained unaffected at day 8 (Figure S1C). All this points to a mild viral myocarditis phenotype in CVB3(H) infection and contrasts with the severe acute systemic inflammatory response, seen after 3 days. Despite sustained bradycardia, PAR2 cleavage-resistant PAR2-R38E mice no longer showed cardiac output impairment in contrast to WT mice. At day 8, the cardiac output had returned to baseline levels in PAR2-R38E mice, and improvement of the cardiac output was accomplished by elevation of the cardiac preload partially, which was not seen in WT mice (Figure 2I; Table 3). This finding supports the notion that PAR2 signaling compromises restoration of hemodynamics after viral infection.

PAR2 Activation Interferes With Restoration of Liver Tissue Homeostasis

To assess the impact of PAR2 signaling on liver tissue integrity in CVB3(H) infection, we evaluated hepatic tissue damage by histology and biochemistry. At the acute phase after 3 days, we found liver tissue damage, as indicated by severe necrosis and scattered detection of inflammatory foci (Figure 3A; Figure S3). Semiquantitative scoring of liver tissue necrosis was performed, which showed less severe destruction of hepatocytes in PAR2-R38E mice at day 3 (Figure 3B). ASAT (aspartate aminotransferase) and LDH (lactate dehydrogenase) activity in serum were markedly elevated (Figure 3C). After 8 days, as liver tissue injury was resolving, we detected rare instances of single-cell necrosis in PAR2-R38E images, whereas WT mice consistently showed multifocal necrotic areas (Figure 3D), demonstrating more severe acute or ongoing hepatocyte injury. Liver serum enzymology showed that ASAT and LDH levels returned to baseline levels in PAR2-R38E but lesser in WT mice (Figure 3E), indicating improved restoration of liver tissue integrity. Altogether, these findings point to a role of PAR2 signaling in the repair process after liver injury. We confirmed that such PAR2-mediated processes were not directly attributed to viral control. Liver tissue from PAR2-R38E and WT mice had equally high viral titers at day 3. Furthermore, our quantification of infectious viral particles by plaque assay revealed no relevant viral titers in the liver of either WT or R38E mice after 8 days, suggesting effective viral clearance from liver tissue in a PAR2 activation-independent manner (Figures S2 and S9B).

Despite histological and biochemical evidence for liver tissue repair at day 8, CVB3(H)-infected WT mice showed ongoing weight loss and hypoglycemia at this phase. Recently, we demonstrated that CVB3 infection

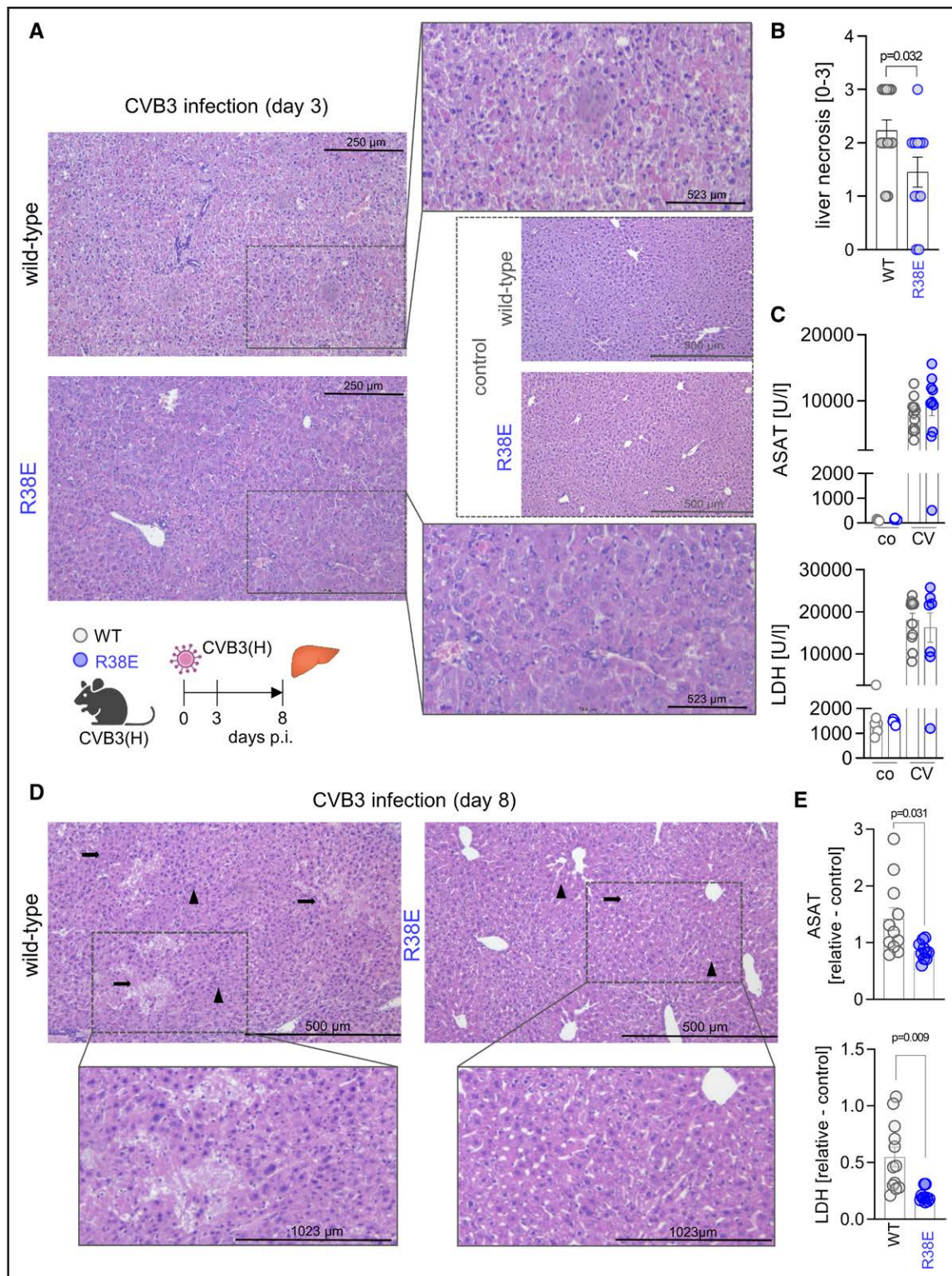


Figure 3. PAR2 (protease activated receptor 2) signaling prolongs restoration of liver tissue injury.

Male PAR2-R38E mice and wild-type (WT) controls infected with coxsackievirus B3 (CVB3[H]). **A**, Representative micrographs from liver tissue sections stained with hematoxylin/eosin at day 3; Sections from uninfected mice (control) show intact liver tissue. **B**, Liver tissue damage assessed using a semiquantitative scoring system ranging from 0 to 3, analyzed after 3 days (WT, n=13; PAR2-R38E, n=11). **C**, Serum activity for ASAT (aspartate aminotransferase) and LDH (lactate dehydrogenase) at baseline and 3 days after infection (control: WT, n=6; PAR2-R38E, n=5; day 3: WT, n=12; PAR2-R38E, n=10). **D**, Representative micrographs from liver tissue sections stained with hematoxylin/eosin after 8 days. Arrows indicate multifocal necrosis areas in WT mice, as well as single-cell necrosis in images from PAR2-R38E mice. Arrow heads mark intact hepatocytes. **E**, Serum activity for ASAT and LDH (WT, n=11; PAR2-R38E, n=10) normalized to baseline measurements. Unpaired *t* tests were used in **E** to calculate the *P* values.

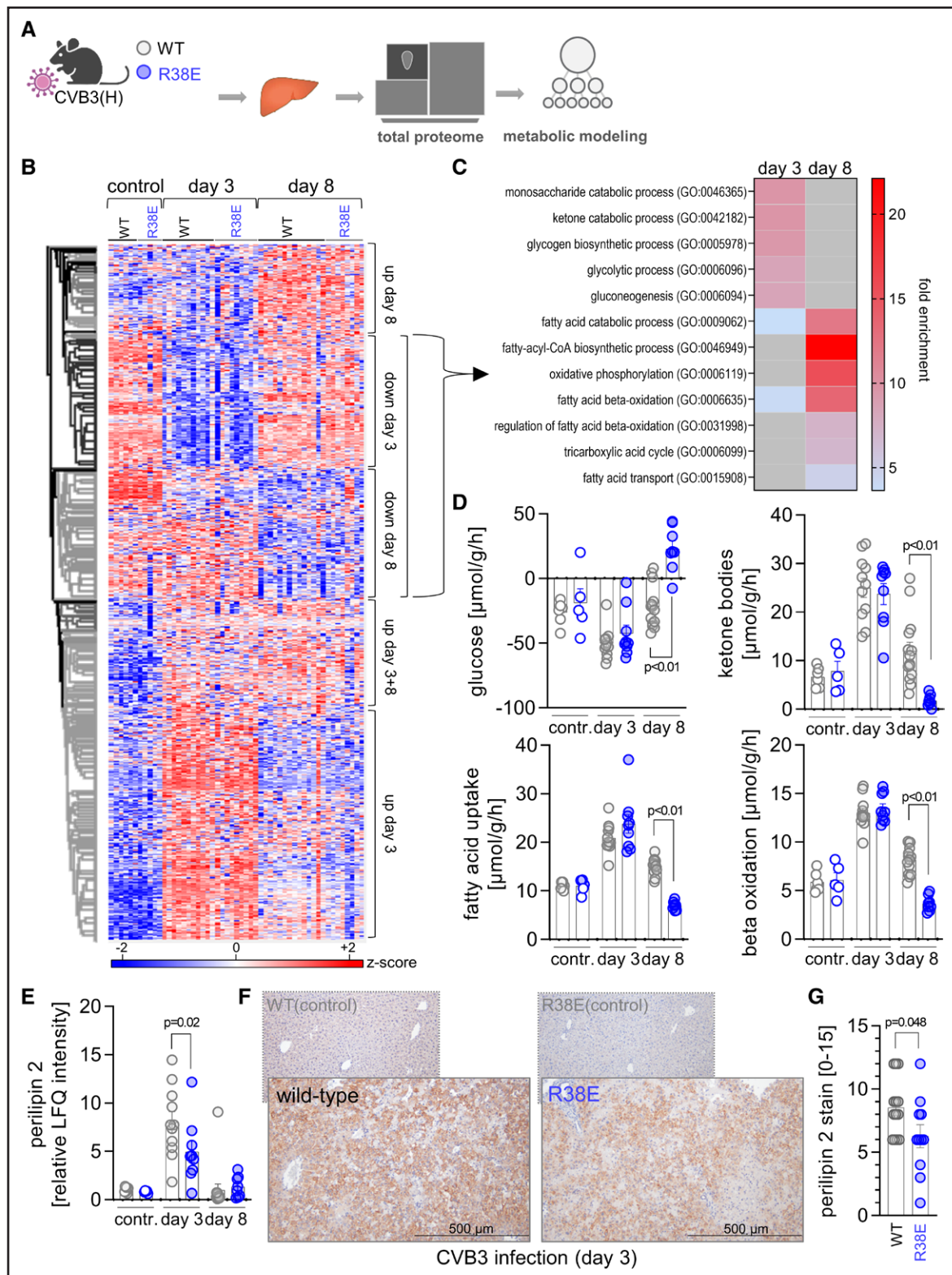


Figure 4. Facilitated restoration of liver metabolism in cleavage-resistant PAR2 (protease activated receptor 2)-R38E mice.

A, Male wild-type (WT) and PAR2-R38E mice infected with coxsackievirus B3 (CVB3[H]). **B**, Liver proteome analyzed by shotgun liquid chromatography–tandem mass spectrometry (LC-MS/MS; control: WT, n=6; PAR2-R38E, n=5; day 3: WT, n=11; PAR2-R38E, n=9; day 8: WT, n=14; PAR2-R38E, n=8) shown as a heatmap of the differential regulation of liver proteins. Relative abundance is based on Z-scored \log_2 -transformed label-free quantification (LFI) intensities. Red indicates proteins with a positive Z score, and blue indicates proteins with a negative Z score. Missing values are colored gray. Clusters are defined according to upregulation and downregulation of proteins 3 and 8 days after infection and at both days 3 and 8. **C**, Heatmap-based clusters were subjected to gene ontology (GO) analysis and selected GO terms of clusters downregulation day 3 or downregulation day 8 are displayed and color coded according to their fold enrichment (*Continued*)

increases the energy expenditure in liver tissue,²⁴ and this is countered by the diminished availability of plasma nutrients in CVB3-infected mice.⁵⁷ Such perturbation of plasma nutrient supply, paired with higher ATP demand, requires an adaptation of central liver metabolism, and this can be affected by quantitative changes in protein abundances of metabolic enzymes.²⁴ To define the role of PAR2 signaling in central liver metabolism, we determined the liver proteome by mass spectrometry in WT and PAR2-R38E mice 3 and 8 days after infection (Figure 4A). DIA-NN mass spectrometry data were analyzed by nonsupervised hierarchical clustering with 2-way ANOVA and Z scoring to generate a heatmap containing 4670 differentially regulated proteins within 5 distinct clusters (Figure 4B; Table S1). GO enrichment analysis of these clusters was performed. The combined clusters of downregulated proteins at 3 or 8 days showed a substantial enrichment of metabolism-linked proteins. As illustrated in Figure 4C (Table S2), we found a significant enrichment of proteins that are involved in carbohydrate metabolism after 3 days and in FA metabolism, as well as in oxidative phosphorylation after 8 days. To further assess the physiological relevance of the observed proteomic changes by the liquid chromatography–tandem mass spectrometry analysis, we integrated protein abundance data of metabolic enzymes into the Hepatokin1 modeling platform, a molecular resolved kinetic model of central liver metabolism,⁵³ which predicts *in silico* organ metabolism. Assuming a 24-hour standard metabolite profile, we computed the mean diurnal metabolic effort of different pathways in the liver after infection. Our simulations show an alteration of liver carbohydrate metabolism toward more gluconeogenesis after 3 days and a shift toward enhanced glycolysis after 8 days, all independent of PAR2 signaling (Figure S4B) and in line with our previous findings for WT mice.²⁴

Regarding FA metabolism, the models computed higher β -oxidation and lower synthesis rates after 3 days. FA synthesis rates returned to baseline conditions in PAR2-R38E mice at day 8, whereas this metabolic pathway remained at reduced levels and decreased further at this stage in WT mice (Figure S4D and S4E), consistent with impaired recovery of liver tissue homeostasis. To evaluate hepatic metabolic function during infection, we used the determined plasma nutrient

concentrations at the respective time points, which deviated significantly from physiological values, as additional input parameters.²⁴ Thereafter, the models computed increased glucose and ketone body production after 3 days, as well as increased FA β -oxidation (Figure 4D). At day 8, however, only mice with a defect in PAR2 signaling showed a return to baseline conditions, consistent with a decreased production of energetic fuels, such as glucose and ketone bodies, by liver tissue. FA uptake and β -oxidation, as well as ketone body production, were within baseline levels in PAR2-R38E mice but remained elevated in WT mice. Moreover, PAR2-R38E mice had lower glucose production and higher glycolysis rates in liver tissue at day 8 (Figure 4D).

Reflecting enlarged lipid droplet (LD) formation in liver at day 3, the metabolic model calculated a higher triacylglycerol content in both WT and PAR2-R38E mice (Figure S3D). LDs are the major lipid storage organelles in liver tissue. Notably, the calculated LD content in liver tissue was higher in WT mice (Figure S4F), pointing toward a PAR2-signaling effect on perilipins, which control LD formation during CVB3 infection.⁵⁸ In fact, perilipin 2 was the most abundantly expressed perilipin in liver tissue at day 3, with label-free quantification intensities being higher in WT mice in comparison to PAR2-R38E mice (Figure 4E). We validated these findings by immunohistochemical visualization of perilipin 2 on liver tissue sections. Figure 4F shows the homogenous, ubiquitous staining pattern for perilipin 2 at day 3 after infection, for which the scoring revealed less abundant and weaker signals in livers from PAR2-R38E mice (Figure 4G). Altogether, the computational simulation of liver metabolism, integrating both the individual metabolic proteome and the shortage of plasma nutrients, demonstrates a central role of PAR2 signaling on reprogramming the central liver metabolism, particularly during the resolution phase of acute infection after 8 days.

Canonical PAR2 Signaling Augments IFN Responses in Liver Tissue

We and others identified a critical role of IFN signaling for metabolic rewiring of carbohydrate and FA metabolism.^{24,59} Based on the causal relationship between IFN responses and tissue damage in CVB3 infection^{19,24} and the demonstrated interference of IFN signaling with the PAR2

Figure 4 Continued. (gray color represents no significant enrichment of the respective GO term at either day 3 or day 8). **D**, Liver proteomes of CVB3-infected WT and PAR2-R38E mice were used for computational analysis in the metabolic model Hepatokin1. Metabolic models for the different conditions were constructed by scaling the maximal activity for each enzyme using the LFQ intensities for each protein obtained from MaxQuant analysis of DIA-NN MS (data-independent acquisition by neuronal network mass spectrometry) data at the respective point in time. For each condition, experimentally determined blood glucose levels were used as model inputs to calculate realistic exchange fluxes. Two-way ANOVA analysis, followed by a Tukey multiple comparison *t* test for multiple-group comparison, was used to calculate the shown *P* values. **E** shows \log_2 -transformed LFQ intensity values for perilipin 2 in infected liver tissue, normalized to uninfected WT controls. Two-way ANOVA analysis, followed by a Tukey multiple comparison *t* test for multiple-group comparison, was used to calculate the shown *P* value. **F** shows the immunohistochemical analysis of perilipin2 (brown) in liver specimens from WT and PAR2-R38E mice after 3 days. The small micrographs are controls from uninfected mice. **G**, Grading of perilipin2 staining distribution and intensity as described in the Methods (WT, n=13; PAR2-R38E, n=11). An unpaired *t* test was used to calculate the shown *P* value.

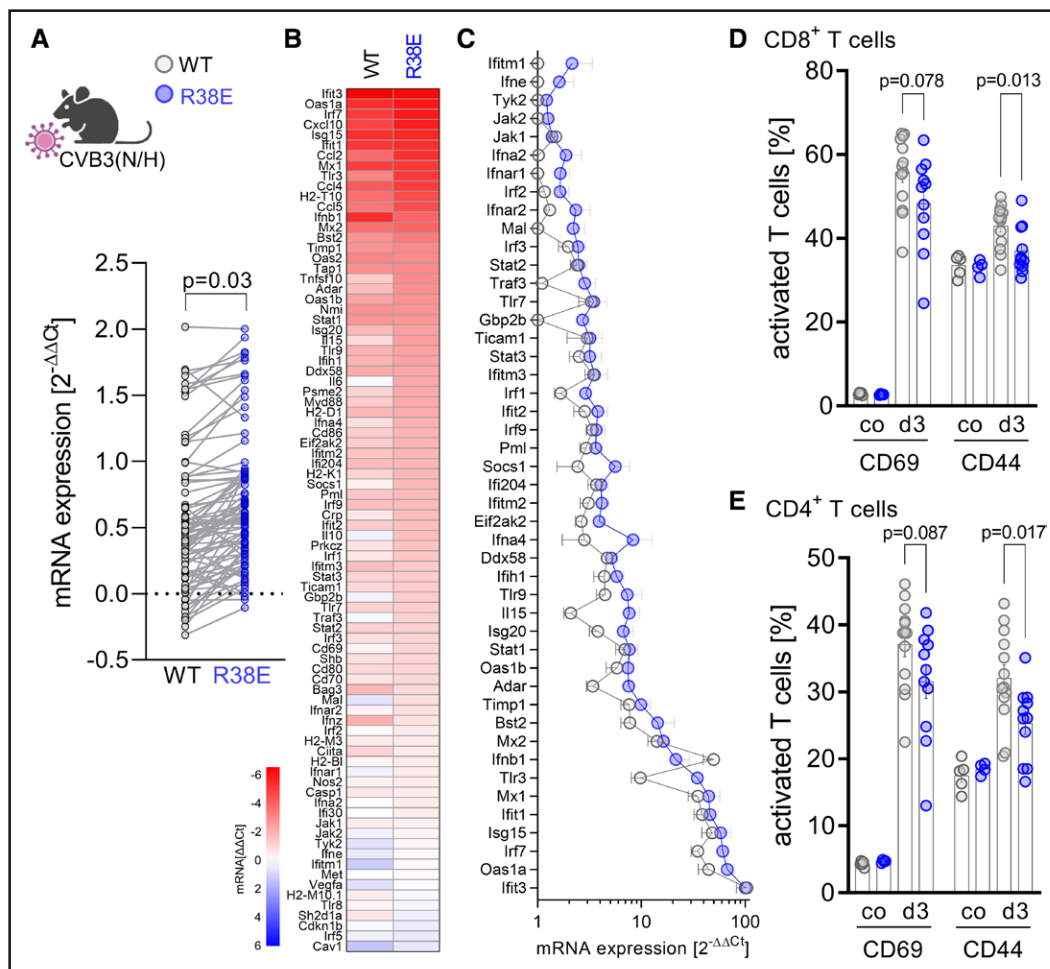


Figure 5. PAR2 (protease activated receptor 2) signaling augments T11FN (type 1 interferon) responses.
A, RNA was extracted from liver tissue obtained from infected male wild-type (WT) and R38E mice (coxsackievirus B3 [CVB3(N)]); day 2; n=6 per group) and profiled for expression of IFN (interferon)-related genes using a mouse T11FN response profiler polymerase chain reaction (PCR) array. Liver RNA from uninfected mice was used as control. Plotted data visualizing the relative expression of each gene in WT and PAR2-R38E mice. The shown *P* value was calculated using an unpaired *t* test. **B**, Heatmap showing the fold gene induction (compared with uninfected tissues) in the liver for infected WT and PAR2-R38E mice. The color code depicts $\Delta\Delta C_t$ (day 2 vs control) values within each genotype; blue corresponds to low and red to high induction levels. **C**, Differential illustration for selected typical T11FN-related genes (ISGs [interferon-stimulated genes]) from the same profiler PCR array. **D** and **E**, Splenocytes stained with fluorochrome-labeled antibodies for cell surface molecules as described in Methods and cells acquired on a FACS (fluorescence-activated cell sorting) Symphony flow cytometer. The gating is presented in Figure S4. WT: control, n=5; day 3, n=13. PAR2-R38E: control, n=4; day 3, n=11. Two-way ANOVA analysis, followed by a Tukey multiple comparison *t* test for multiple-group comparison, was used to calculate the shown *P* values.

platform,²⁹ we profiled the regulation of the IFN response by PAR2 signaling in liver tissue with quantitative PCR arrays. We found robust induction of IFN-responsive gene expression in liver tissue at the acute stage. Notably, the IFN signature was enhanced in liver tissue from PAR2-R38E mice with cleavage-resistant PAR2 (Figure 5A through 5C). Deficient PAR2 signaling most prominently affected IFN-stimulated genes, such as ISG15 and IFIT, with overall enhanced transcriptional activity for ISGs (IFN-stimulated genes) in PAR2-R38E mice (Figure 5B and 5C). As T-cell immunity exerts deleterious effects, we profiled T-cell activation for both CD4⁺ and CD8⁺ T cells, by quantifying the activation markers CD69 and CD44 by flow cytometry in the spleen. CD44 is best known as a critical regulator of immune cell migration, including the recruitment of T cells to sites of infection.⁶⁰ We

detected CD69 and CD44 expression in about 50% of the CD8⁺ T-cell and in about 30% of the CD4⁺ T-cell population at day 3 (Figure 5D and 5E). In comparison to WT mice, cleavage-resistant PAR2-R38E mutants showed a reduced proportion of CD44⁺ T cells. We conclude that PAR2 signaling shifts cellular responses in CVB3 infection toward proinflammatory signatures, whereas IFN signatures were either suppressed or left unaffected.

PAR2-β-Arrestin Axis Perpetuates the Hypodynamic Phase in CVB3 Infection

We next focused on downstream PAR2 activation and investigated the role of β-arrestin recruitment to the PAR2 signaling platform. Therefore, we studied

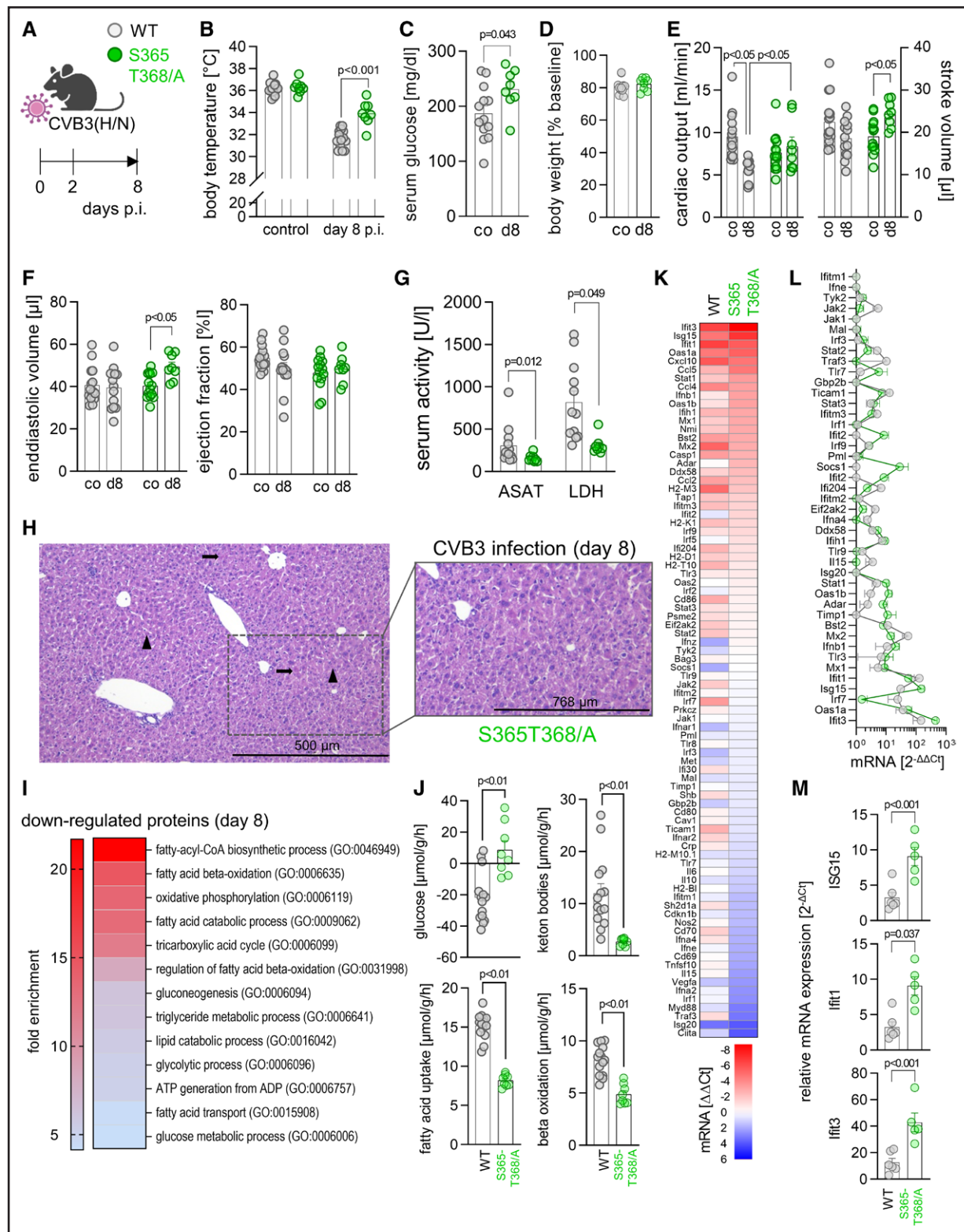


Figure 6. Adverse effects of the PAR2 (protease activated receptor 2) signaling platform due to β -arrestin coupling.

A, Male wild-type (WT) and PAR2- β -arrestin coupling incompetent PAR2-S365T368/A mice were infected with coxsackievirus B3 (CVB3[H]), and the mice were measured at the indicated time points. **B**, Body temperatures (WT, $n=14$; PAR2-S365T368/A, $n=8$). **C**, Serum glucose levels (WT, $n=14$; PAR2-S365T368/A, $n=8$) of control samples and after 8 days. **D**, Body weight change, **E** and **F**, Cardiac performance assessed by echocardiography with Vevo3100 before infection and after 8 days (WT, $n=13$; PAR2-S365T368/A, $n=8$) is shown. **G**, Serum activity of lipase, ASAT (aspartate aminotransferase), and LDH (lactate dehydrogenase) after 8 days (WT, $n=12$; PAR2-S365T368/A, $n=8$). **B**, **E**, and **F**, Two-way ANOVA analysis followed by a Tukey multiple comparison t test for multiple-group comparison. **C**, **D**, and **G**, Unpaired t test. **H**, Representative micrographs from liver tissue of PAR2-S365T368/A mice stained with hematoxylin/eosin after 8 days. (Continued)

phosphorylation-deficient PAR2-S365T368/A mice with mutated PKC phosphorylation sites, rendering the PAR2 C-terminal intracellular domain incapable of β -arrestin recruitment (Figure 6A). Mutating this phosphorylation site is permissive with proteolytic canonical PAR2 signaling, for example, in tumor cells *in vivo*.² We focused our analysis on the recovery stage of CVB3 infection (day 8) and, consistent with our findings in PAR2-R38E mice, we observed higher blood glucose concentrations and elevated body temperatures in PAR2-S365T368/A mice in comparison to their WT controls (Figure 6B and 6C). PAR2-S365T368/A mice showed the same drop of the body weight as WT controls (Figure 6D). Quantification of cardiac inflammation by flow cytometry-based counting of infiltrating immune cells showed a mild inflammatory response in cardiac tissue and, with the exception of slightly reduced macrophages, an equivalent immune cell abundance in hearts from PAR2 S365T368/A and WT mice (Figure S1D). The cardiodepressant effects documented at day 8 in CVB3(H) infection with sustained bradycardia and lower output due to PAR2 signaling were recapitulated in WT controls. In contrast, PAR2- β -arrestin coupling-deficient PAR2-S365T368/A mice showed compensatory aspects that mitigated the hypodynamic condition and elevated the cardiac output similarly to PAR2-R38E mice. PAR2-S365T368/A mice had an elevated cardiac preload, and, despite low heart rates, this enabled a restoration of the cardiac output similar to the values measured before infection (Figure 6E and 6F; Table 4).

We next investigated the relevance of the PAR2- β -arrestin axis for resolution of liver tissue injury at day 8. ASAT and LDH serum activities, representative for hepatocyte injury, were reduced in PAR2-S365T368/A mice (Figure 6G), and this corresponded to histological detection of overall intact liver tissue with minor single-cell necrotic lesions (Figure 6H) in comparison to multifocal injury in WT mice (Figure S3B). Despite this evidence for a restored liver phenotype, compiling of liver proteomics into a heatmap (Figure S6; Table S3) and the consecutive GO enrichment analysis revealed metabolic pathways highly enriched within the cluster of downregulated

proteins in PAR2-S365T368/A mice at day 8 (Figure 6I; Table S4). We found a prominent abundance among the downregulated proteins that are involved in FA synthesis and β -oxidation, as well as oxidative phosphorylation, resembling the metabolic perturbations shown above for the subacute phase (Figure 4C). We then used physiological plasma concentrations as input parameters to integrate the proteomics-based expression levels for the various metabolic enzymes and regulatory proteins into Hepatokin1 liver metabolism models. For PAR2-S365T368/A mice, we computed FA uptake and β -oxidation, as well as ketone body production to be reduced in comparison to WT controls. Moreover, mice with a defect in the PAR2- β -arrestin axis showed lower glucose production rates, and, in fact, some animals consumed glucose instead and had no or only low gluconeogenesis activity (Figure 6J). Since these findings corresponded to the results presented for PAR2-R38E mice, we conclude that the adverse effects of PAR2 signaling on tissue repair were controlled, at least in part, by PAR2- β -arrestin coupling.

Finally, we explored the relevance of this axis for control of the IFN response at the acute phase. We, therefore, profiled IFN signatures in liver tissue with quantitative PCR arrays and found that the vast majority of highly induced ISGs at day 2 were enhanced in PAR2-S365T368/A mice more strongly (Figure 6K and 6L). We profiled the highest induced ISGs with known relevance in CVB3 infection by quantitative PCR and found enhanced mRNA expression in liver tissue from PAR2-S365T368/A mice (Figure 6M). This demonstrates that the PAR2- β -arrestin axis promoted hemodynamic compromise, documenting interference of the PAR2- β -arrestin axis with tissue repair in CVB3 infection.

Evidence for TF-FVIIa-Mediated PAR2 Signaling in CVB3 Infection

To define putative therapeutic implications of our findings, we pursued the hypothesis that the TF pathway through TF-FVIIa complex-mediated PAR2 rather than FXa-mediated PAR2 activation influenced CVB3 infection.

Figure 6 Continued. Arrows indicate single-cell necrosis, and arrow heads mark intact hepatocytes. **I**, Liver proteome from day 8 WT and PAR2-S365T368/A mice (control: WT, n=6; PAR2-S365T368/A, n=4; day 8: WT, n=15; PAR2-S365T368/A, n=9) analyzed by shotgun liquid chromatography-tandem mass spectrometry (LC-MS/MS). Heatmap-based cluster downregulation day 8 (Figure S6) gene ontology (GO) analysis and selected GO terms are displayed color coded according to fold enrichment. **J**, Liver proteomes of CVB3-infected male WT and PAR2-S365T368/A mice (WT, n=14; PAR2-S365T368/A, n=8) used for computational analysis in the metabolic model Hepatokin1. Scaling the maximal activity for each enzyme using the label-free quantification (LFO) intensities for each protein obtained from MaxQuant analysis of DIA-NN MS (data-independent acquisition by neuronal network mass spectrometry) data. For each condition, experimentally determined blood glucose levels were used as model input to calculate realistic exchange fluxes. Unpaired *t* test. **K**, RNA extracted from liver tissue obtained from infected WT (n=6) and PAR2-S365T368/A (n=5) mice (CVB3[N], day 2). RNA profiling of IFN (interferon)-related genes using a mouse T11FN response profiler polymerase chain reaction (PCR) array. Liver RNA from uninfected mice used as controls. Heatmap showing the fold gene induction (compared with uninfected tissues) in the liver. Color code depicts $\Delta\Delta$ Ct values (day 3 vs control) within each genotype; blue corresponds to low and red to high levels of induction. **L**, Differential illustration of selected ISGs (interferon-stimulated genes) from the same profiler PCR assay. **M**, Quantitative PCR analysis for the most abundant ISGs, namely ISG15 (IFN-stimulated gene of 15 kDa), Ifit1, and Ifit3 (WT, n=6; PAR2-S365T368/A, n=5). Unpaired *t* tests were performed, and respective *P* values are shown.

Table 4. Mitigated Hemodynamic Compromise in PAR2- β -Arrestin Coupling Mutants (PAR2-S365T368/A Mice)

| | WT | | PAR2-S365T368/A | |
|---------------------------------------|----------------|-----------------|-----------------|-----------------|
| | Baseline | Day 8 | Baseline | Day 8 |
| Heart rate, bpm | 423 \pm 8 | 298 \pm 9* | 399 \pm 12 | 292 \pm 16* |
| Trace EF, % | 54.9 \pm 1.4 | 49.8 \pm 3.0 | 47.8 \pm 2.0 | 49.7 \pm 2.3 |
| Cardiac output, mL/min | 9.5 \pm 0.7 | 5.5 \pm 0.3*† | 7.6 \pm 0.6 | 8.4 \pm 1.1 |
| Stroke volume, μ L | 22.5 \pm 1.5 | 18.6 \pm 1.3 | 19.1 \pm 1.1 | 24.4 \pm 1.1* |
| Vol d, μ L | 40.7 \pm 2.2 | 39.5 \pm 2.8 | 40.4 \pm 1.6 | 49.4 \pm 2.2* |
| LVID-d, mm | 3.6 \pm 0.1 | 3.7 \pm 0.1 | 3.7 \pm 0.1 | 3.7 \pm 0.1 |
| LVID-s, mm | 2.6 \pm 0.1 | 2.7 \pm 0.1 | 2.7 \pm 0.1 | 2.8 \pm 0.1 |
| MV E, mm/s | 745 \pm 30 | 525 \pm 36* | 644 \pm 24 | 551 \pm 32 |
| MV _{decel} [†] , ms | 20.3 \pm 1.4 | 34.8 \pm 2.8* | 25.3 \pm 1.4 | 30.5 \pm 3.9 |
| IVRT, ms | 19.7 \pm 0.6 | 29.7 \pm 2.1* | 20.9 \pm 0.4 | 29.2 \pm 2.0* |

Mice were subjected to echocardiography (WT, n=15; PAR2-S365T368/A, n=14; all males). Mice were infected with CVB3(H), and for these animals, a second echocardiogram was obtained after 8 d (WT, n=9; PAR2-S365T368/A, n=8; all males). Data are mean \pm SEM. Two-way ANOVA was performed followed by a Tukey multiple comparison test. Mitral valve E velocity was determined by pulse-wave Doppler at mitral valve. CVB3 indicates coxsackievirus B3; EF, ejection fraction; IVRT, isovolumic relaxation time; LVID-d, left ventricular internal diameter at diastole; LVID-s, left ventricular internal diameter at systole; MV_{decel}[†], mitral valve deceleration time; MV E, mitral valve E velocity; PAR2, protease-activated receptor 2; Vol d, volume at diastole; and WT, wild type.

*Significant differences ($P<0.05$) between WT and PAR2-S365T368/A 8 d after infection.

†Significant differences ($P<0.05$) between WT and PAR2-S365T368/A 8 d after infection.

This finding strengthened the notion that TF-FVIIa complex formation and the resulting PAR2 cleavage by FVIIa promoted physiologically relevant PAR2 activation. To investigate the proposed role of TF-FVIIa complex in activating PAR2 signaling, we used a TF pathway-directed inhibitor, the NAPc2. NAPc2 interacts with the TF-FVIIa complex through its ascaris-type inhibitory domain, and another domain binds X/Xa, independently of its active site.^{39,61} In this stabilized TF-FVIIa-Xa complex, NAPc2 blocks FVIIa proteolysis, but the ability of FXa to cleave PAR2 or other substrates remains intact.^{62,63} Given that FXa in the ternary complex has no impact on CVB3 infection (Figure 1), NAPc2, therefore, provides a powerful tool to specifically inhibit TF-FVIIa-mediated PAR2 signaling. As a model system, first, we switched to heart disease-susceptible A/J mice instead of C57BL/6 mice and infected these mice with CVB3(N). This CVB3 model is suited to explore the proposed effects at the subacute phase, with more emphasis on cardiac inflammation,⁴² in comparison to CVB3(H)-infected C57BL/6 mice. Daily NAPc2 treatment was initiated in A/J mice simultaneous with CVB3 infection. Notably, CVB3(N) infection resulted, as reported previously,^{42,55} in less cardiac output due to perpetuated preload deficit, and this was at least partially compensated by NAPc2. Both the stroke volume and the cardiac output were reduced in the sham group more strongly (Figure 7B; Table 5). Myocarditis phenotyping, which comprised of histological evaluation (Figure 7E and

7F) and quantification of infiltrating immune cells by flow cytometry, showed equivalent virus-triggered responses in both groups (Figure S7A). These findings corroborate the notion that PAR2 signaling mediates its physiological function independent of viral control in the heart tissue (Figures S6B and S13B). In support of the conclusion that NAPc2 treatment compensated for the infection-triggered preload deficit found in A/J mice, the myocardial performance index (Tei index), a Doppler index of combined systolic and diastolic myocardial performance, and the LV ejection fraction, both determined by echocardiography, showed such beneficial activity in the NAPc2 treatment group (Figure 7C; Table 5). These alterations at least partially explained the higher stroke volume in this group. Consistent with lower lung fluid content, as a sign of less pulmonary congestion (Figure 7D), the effects in the NAPc2 treatment group counteracted infection-triggered hypodynamic conditions and pointed to the physiological relevance of TF-FVIIa-PAR2 signaling in blocking such responses. Further evidence for the intimate link of the TF-FVIIa complex with PAR2 signaling in CVB3 infection came from elevated blood glucose levels and higher body temperatures in the NAPc2 treatment group (Figure 7G and 7H), and this corroborated the notion of perturbed tissue repair due to TF-FVIIa-mediated PAR2 cleavage. As a next step, we infected WT mice on a C57BL/6 N background with CVB3(H) and treated them with NAPc2 for 8 days (Figure 7I). As expected from our previous data, acute liver tissue injury had transferred to the restoration phase at this point in time, with liver tissue integrity being indeed more pronounced in the NAPc2 treatment group (Figure 7J and 7K). Moreover, we found less severe hypothermia during the acute phase in the NAPc2 group, without relevant effects after 8 days (Figure 7L). The blood glucose concentration was not affected by NAPc2 (Figure 7M). The myocarditis phenotype, triggered by virus infection, was less pronounced in the NAPc2 treatment group, revealing less severe myocarditis scores, despite similar virus titer (Figure 7N and 7O; Figure S6D and S6E). Altogether, these data confirm the role of TF-FVIIa-PAR2 signaling in CVB3 infection.

DISCUSSION

PAR2 is a sensor of TF-engaged coagulation proteases, and cleavage of its extracellular N-terminal domain generates a tethered ligand that induces G-protein signaling with a variety of downstream pathways. Herein, PAR2 cooperates with PAMP-related host receptor signaling, blunting the expression of TLR3/IRF3-driven genes.¹⁰ Upon PAR2 activation, the intracellular recruitment of β -arrestin uncouples PAR2 and negatively regulates G-protein signaling.⁶⁴ In this study, we demonstrate PAR2-sustained hypodynamic and metabolic compromise in CVB3 infection, a stimulant of RNA-sensing TLRs, despite efficient antiviral immune responses

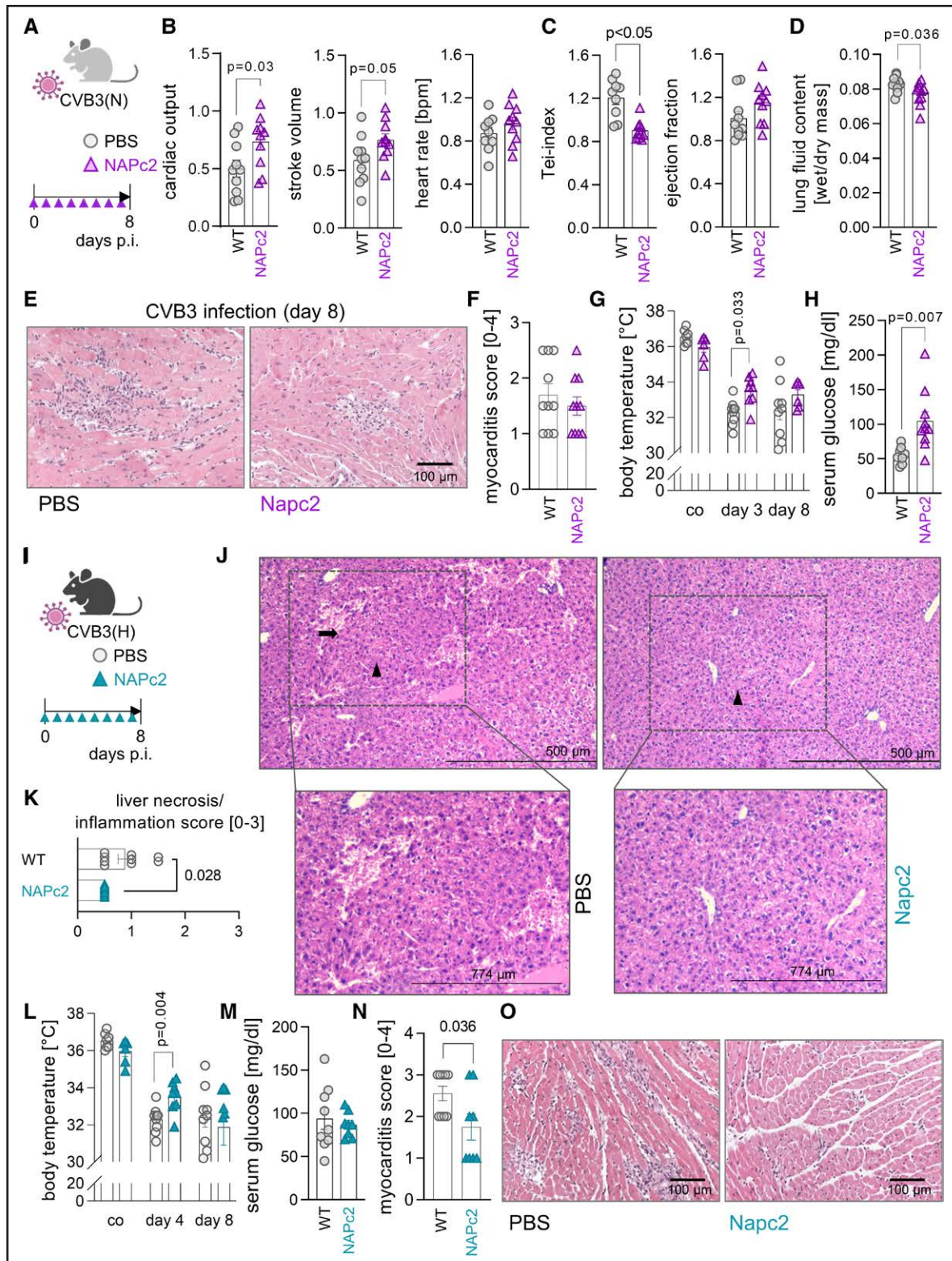


Figure 7. NAPc2 (nematode anticoagulant protein C2) mitigated inflammatory compromise in coxsackievirus B3 (CVB3) infection.

A, Male A/J mice infected with 1×10^4 pfu of CVB3(N), daily injections with NAPc2 (1 mg/kg body weight) starting at the day of infection. **B** and **C**, Cardiac performance was calculated by echocardiography at baseline and after 8 days ($n=10$ per group). Relative alterations for each infected animal in comparison to its baseline measurement are shown, and unpaired t test was performed. **D**, Lung fluid content after 8 days ($n=10$ per group). Unpaired t test. **E**, Representative micrographs from paraffin-embedded cardiac sections stained with hematoxylin and eosin and **(F)** scoring of these sections (each dot represents a different animal). **G**, Body temperature at baseline (vehicle, $n=7$; Napc2, $n=6$) and after infection (day 2: vehicle, $n=9$; Napc2, $n=9$; day 8: vehicle, $n=9$; Napc2, $n=6$). Two-way ANOVA analysis followed (*Continued*)

to control the viral burden. We discovered cross talk between the TF-FVIIa, PAR2 activation, and intracellular recruitment of β -arrestin to PAR2 independent of FXa-PAR2 signaling. Drop of plasma nutrient supply,⁵⁷ paired with increased energy expenditure in CVB3 infection,²⁴ required an adaptation of central liver metabolism, with elevated glucose and ketone body production, increased FA β -oxidation, accomplished regardless of PAR2 engagement. At this phase, hepatocytes trap the virus and protect other cells at the expense of their own survival.⁵⁸ Remarkably, the PAR2- β -arrestin axis altered this cellular response in liver tissue and reduced IFN-related ISG signatures. Moreover, PAR2- β -arrestin signaling sustained hypoglycemia and thereby promoted constant glucose production by liver tissue during the subacute stage of infection, consistent with wasting. Based on impaired resolution of liver tissue injury, these data indicate that PAR2 signaling via β -arrestin coupling interferes with tissue regeneration, which contrasts with data implicating PAR2 in the regeneration after toxic liver injury.² PAR2-dependent immune signaling in CVB3 infection contributed to prolonged hypodynamic conditions with reduction of the cardiac output, hypothermia, and increased mortality. Similarly, TF-PAR2 signaling has been linked to ischemia-mediated heart failure and fibrosis.⁶⁵ We propose coagulation-independent inhibition of TF-FVIIa-PAR2- β -arrestin signaling as a therapeutic approach for mitigating metabolic and inflammatory disturbances in CVB3 infection.

The coagulation and innate immune response systems interact to form an integrated defense against tissue injury and infection. TF—the initiator of the coagulation cascade—is induced in endothelial and myeloid cells by inflammatory mediators released by viral infection.^{66,67} PAR2 is the central mediator for the context-specific effects of the upstream coagulation proteases FVIIa and FXa in the TF pathway. In cancer immunology, FXa-PAR2 signaling exerts immunosuppressive activity, promoting tumor growth, but anticoagulants blocking FXa can reverse these PAR2 effects and stimulate the expansion of tumor-destructive cytotoxic T cells.³⁶ In contrast, FXa-PAR2 signaling during CVB3 infection did not show a substantial immune-regulating effect. In fact, mice harboring the PAR2-FXa cleavage-insensitive G37I mutant showed similar characteristics as WT mice, suggesting either that there is no biologically relevant contribution of the FXa-PAR2 axis or there are compensatory

effects accomplished by alternative PAR2 activators. TF-FVIIa-FXa-PAR2 signaling depends on interactions between the FXa γ -carboxyglutamic acid domain with EPCR (endothelial cell protein C receptor).⁶⁸ Therefore, the absence of relevant FXa-PAR2 signaling might be explained by nonoverlapping expression profiles for TF and EPCR and a lack of spatial proximity between the receptors on cell types relevant during CVB3 infection.

In contrast, specific blockade of the TF-FVIIa complex linked the TF pathway directly to the identified immune-related suppressive PAR2 signal. A specific inhibitor of TF-FVIIa-mediated PAR2 cleavage, the hookworm-derived protein NAPc2, induced a partial reversal of the hypodynamic condition during CVB3 infection, illustrating not only the importance of the TF-FVIIa-PAR2 axis but also suggesting a putative therapeutic modality. Similar to our study, the deleterious effects of overactivation of the coagulation cascade by TF was observed in other infection models, such as Ebola virus-induced hemorrhagic fever, and effectively prevented by NAPc2.⁹ More recently, NAPc2 was also evaluated in COVID19 and showed anticoagulant efficacy without apparent interference with antiviral immunity.⁶⁹

Whereas our study clearly defines the physiological importance of the TF-FVIIa-PAR2 axis in CVB3 infection, the phenotype differs from what was reported by Weithauser et al in PAR2^{-/-} mice. The investigators used the CVB3(N) strain to induce myocarditis and observed a reduction of viral load and myocardial inflammation.²⁹ We found PAR2 signaling to be irrelevant for viral control or the inflammation of the heart infection triggers. These differences might arise from alterations in the tissue-resident macrophages, known for PAR2-regulated inflammatory activation in the context of DNA clearance in the fetal liver.⁷⁰ Such effects could activate antiviral programs in noninfected cells and exert preconditioning properties that might explain the lower viral burden in PAR2-deficient mice.²⁹ Whereas phenotypes of PAR2-deficient and PAR2 cleavage-resistant mice typically overlap, disruptions of PAR2/PAR1 by an individual knockout can have profound effects on the signaling platform and protease responses.³¹ Our data indicate that those previously demonstrated effects of PAR2 deficiency on CVB3 myocarditis were, at least in part, caused by effects unrelated to canonical proteolytic activation and direct signaling of PAR2.

We show that the adverse effects due to immune activation by viral RNA in both CVB3(N) and CVB3(H)

Figure 7 Continued. by a Tukey multiple comparison *t* test for multiple-group comparison. **H**, Serum glucose concentration after 8 days (vehicle, n=8; NAPc2, n=10). Unpaired *t* test. **I**, Wild-type (WT) mice (Par2^{fl/fl} mice on C57BL/6 N background) infected with CVB3(H) and subjected to daily injections with NAPc2 (1 mg/kg body weight) initiated at the day of infection (PBS, n=9; NAPc2, n=8). **J**, Representative micrographs from liver tissue sections stained with hematoxylin/eosin at day 8. Arrows indicate multifocal necrosis areas, and arrow heads show hepatocytes. **K**, Liver tissue damage assessed using a semiquantitative scoring system ranging from 0 to 3, analyzed after 8 days (WT, n=9; Napc2, n=7). Unpaired *t* test. **L**, Body temperature at baseline (vehicle, n=7; Napc2, n=6) and after infection (day 4: vehicle, n=9; Napc2, n=8; day 8: vehicle, n=9; Napc2, n=8). **M**, Serum glucose concentration after 8 days (vehicle, n=9; NAPc2, n=8). **N**, Scoring of cardiac sections stained with hematoxylin and eosin (each dot represents a different animal). **O**, Representative micrographs from paraffin-embedded cardiac sections.

Table 5. Cardiac Performance in NAPc2-Treated A/J Mice After CVB3 Infection

| | Sham | | NAPc2 | |
|--------------------------|-----------|------------|-----------|-----------|
| | Baseline | Day 8 | Baseline | Day 8 |
| Heart rate, bpm | 409±19 | 343±26 | 380±14 | 366±22 |
| Trace EF, % | 53.4±1.1 | 53.7±3.5 | 49.9±1.8 | 57.5±3.0* |
| FAC, % | 48.4±1.6 | 48.8±3.5 | 42.1±1.0 | 50.1±2.9† |
| MPI | 0.75±0.02 | 0.91±0.05† | 0.85±0.04 | 0.77±0.02 |
| Stroke volume, µL | 22.1±0.6 | 13.0±1.5† | 19.6±1.2 | 15.0±1.0† |
| Cardiac output, mL/min | 9.0±0.5 | 4.5±0.7† | 7.5±0.7 | 5.5±0.5† |
| Vol d, µL | 41.4±1.1 | 25.2±2.5† | 39.0±1.4 | 26.3±1.7† |
| LVID-d, mm | 3.5±0.1 | 2.9±0.2† | 3.5±0.1 | 3.0±0.1† |
| LVID-s, mm | 2.5±0.1 | 2.1±0.2† | 2.6±0.1 | 2.1±0.1† |
| MV E, mm/s | 823±38 | 502±62† | 716±45 | 567±54 |
| MV _{decel} , ms | 25.3±1.5 | 28.0±2.3 | 30.2±2.1 | 30.6±2.2 |
| IVRT, ms | 17.9±0.7 | 22.5±1.3† | 20.7±1.3 | 20.3±1.3 |

A/J mice were subjected to echocardiography (Vevo3100) to monitor left ventricular function (n=10 mice per group; all males). Daily i.p. treatment with NAPc2 or sham (PBS) was initiated on the day of infection with CVB3(N), and a second echocardiogram was obtained after 8 d. Data are mean±SEM. Two-way ANOVA was performed followed by a Sidak multiple comparison test, if indicated. Mitral valve E velocity was determined by pulse-wave Doppler at mitral valve. CVB3 indicates coxsackievirus B3; EF, ejection fraction; FAC, fractional area change; i.p., intraperitoneal; IVRT, isovolumic relaxation time; LVID-d, left ventricular internal diameter at diastole; LVID-s, left ventricular internal diameter at systole; MPI, myocardial performance index; MV_{decel}, mitral valve deceleration time; MV E, mitral valve E velocity; NAPc2, nematode anticoagulant protein C2; and Vol d, volume at diastole.

*t test; significant differences ($P<0.05$).

†Significant differences ($P<0.05$) within each group, triggered by infection.

infection remained evident during the subacute phase, with an aggravated T2 phenotype due to TF-FVIIa-PAR2 signaling. Under conditions of proper innate immune effector activity with effective pathogen elimination,^{17,22,24} as is the case for the WT C57BL/6 and A/J mice used in this study, hypodynamic compromise with metabolic perturbation, wasting, and impairment of cardiac output defines the phenotype in CVB3 infection.^{42,71,72} Consistent with perturbed organ repair at T2 due to PAR2 activation, this study indicates proinflammatory TF-FVIIa-PAR2 signaling in mice with a shift of cellular immune activation toward less ISG production. Although the release of chemokines/cytokines was not affected by canonical PAR2 cleavage at T1, we suspect that the timing of their production might influence to what extent these immune-modulatory molecules affect the outcome of CVB3 infection.⁷³ In fact, our previous studies showed a time- and context-specific efficacy for the reversal of the T2 phenotype by anti-inflammatory molecules, such as immunoproteasome inhibitors, during CVB3 infection. The protective effects by this anti-inflammatory drug relied on intact propagation of innate antiviral immunity^{42,74,75} and required constant inhibitory activity starting directly with the infection.^{42,55} We propose that upon recognition of viral pathogen motifs, such as CVB3 RNA, by the host's PRR, canonical PAR2 signaling converges

with intracellular PRR pathways, and this leads to aggravation of tissue injury in viral infection.

Mechanistically, there is compelling evidence for a central role of MAP (mitogen-activated protein kinase) kinase signaling at the intersection of TLR and PAR2 signaling in CVB3-triggered inflammation. CVB3 infection activates MAP kinase ERK1/2 phosphorylation,⁷⁶ and the same pathway endows TLR-activated cells with enhanced proinflammatory signaling properties leading to T-cell activation.^{42,71} Moreover, mitigating the hypodynamic condition in CVB3 infection, for example, by treatment with immunoproteasome inhibitors, relies on prematurely terminating ERK1/2 activation.^{42,71,77} On the other hand, TF-FVIIa-PAR2 signaling prolongs endosomal MAP kinase ERK1/2 signaling.⁵ Hence, we speculate that phenotypic attenuation with improved tissue repair and less hemodynamic compromise in PAR2 cleavage-resistant mice, as shown here, involves lack of PAR2-mediated activation of ERK1/2 activity. This assumption is strengthened by consistent findings in PAR2- β -arrestin coupling-deficient mice. Importantly, recruitment of β -arrestin to PAR2 supports cytosolic ERK1/2 scaffolding,³⁷ and this aspect is lost in PAR2-S365T368/A mice. Both PAR2-R38E and PAR2-S365T368/A mice showed consistent resolution of acute CVB3 infection with improved cardiac output, facilitated restoration of metabolic perturbation and resolution of the hypodynamic condition at T2. Hence, the complementary phenotype in infected PAR2-R38E and PAR2-S365T368/A mice argues in favor of the proposed role of ERK1/2 activation in CVB3 infection.

Recent work in obese rodent models identified PAR2 as a new regulator of hepatic metabolism that links liver inflammation with glucose, lipid, and cholesterol metabolism.^{78,79} PAR2 activation increases the lipid uptake⁸⁰ and stimulates lipogenesis,⁷⁹ promotes inflammation of visceral adipose tissue and liver,⁶⁴ and enhances gluconeogenic and lipogenic pathway transcripts, partially due to blunted activation of AMPK (AMP-activated protein kinase)⁸¹ and stimulation of the Gi-Jnk1/2-SREBP-1c pathways.⁷⁹ PAR2 signaling in CVB3 infection stimulated perilipin 2 production and enhanced liver LD formation. LD provides a source of fuels for the structural development of replication organelles during CVB3 infection.⁸² In cell culture studies, the induction of LDs occurs early and transiently postviral infection as a result of PRR signaling, consistent with the return to baseline condition shown here at T2. Faced with the challenge of a plasma nutrient shortage coupled with a higher energy demand,²⁴ compensation of hypoglycemia at the T1 phase in CVB3 infection involved PAR2-independent enhanced gluconeogenesis^{42,3} and ketone body formation by liver tissue. Corresponding to higher ATP demand at T1, the computational simulation of liver metabolism calculated higher FA β -oxidation rates. With the enhanced production of acetyl-CoA by FA oxidation, there is also an increased

substrate availability for ketone body production. Loss of body mass in CVB3 infection reflects mobilization of endogenous resources and is consistent with the demonstrated shift in the liver's metabolic program.

PAR2- β -arrestin signaling substantially affected liver metabolism, particularly at the T2 phase in CVB3 infection. The Hepatokin1 model integrates effects that stem from altered protein abundancies in the metabolic proteome and evaluates the biological relevance of such alterations.⁵³ Assuming a standardized nutrient supply at T2, the models revealed a shift from glucose production toward glucose consumption. In fact, this metabolic shift is consistent with our previous findings, where we demonstrated enhanced glucose utilization by liver tissue to be partially dependent on ISG15.²⁴ Here, we showed higher ISG15 mRNA expression in liver tissue with abolished PAR2- β -arrestin signaling, which points toward a putative correlation of PAR2-directed signaling with the respective metabolic reprogramming in the liver. Importantly, despite liver tissue acquired glucose consuming properties for ATP production at T2, further calculations, which we based on the actual serum glucose concentrations, demonstrated that only mice with a PAR2- β -arrestin signaling defect used glucose for their energetic demand. In contrast, hypoglycemia at T2 in WT mice enforced ongoing liver gluconeogenesis at this stage. WT mice had an ongoing need for ketone body production at T2 as well, and this was reflected by constantly elevated FA β -oxidation rates, fueling this process and supplying liver tissue with ATP. In contrast, mice with a defect in their PAR2- β -arrestin signaling showed baseline conditions without any demand for ketone body formation. Such metabolic perturbation with permanently increased production of energetic fuels from endogenous sources, for example, by gluconeogenesis and ketogenesis, explains the higher body weight loss in WT mice in comparison to PAR2 cleavage-resistant mice. The ongoing demand for endogenous glucose production, provided by liver gluconeogenesis, is fueled by amino acids that are primarily supplied by the breakdown of muscle protein by autophagy. Thus, the hypodynamic condition with metabolic perturbation triggered by the PAR2- β -arrestin axis stimulates the wasting processes during CVB3 infection.

Closely connected to energy expenditure, thermoregulation and cardiac performance are other fundamental homeostatic functions that were disturbed by the TF-FVIIa-PAR2- β -arrestin axis in CVB3-infected mice. The ongoing hypothermic condition that we detected due to TF-FVIIa-PAR2- β -arrestin signaling indicates energy exhaustion and is an established predictor of mortality in sepsis.⁸³ Moreover, the cardiac dysfunction that we documented during CVB3 infection in this study is pronounced and characterized by elements of hypovolemic and distributive shock. Much of the reduction of the cardiac output in CVB3 infection at T1 in our study was due to reduced preload, reminiscent of the conditions found

in cecal ligation and puncture sepsis models. Reductions in preload lower the stroke volume represented by identical ejection fractions,⁸⁴ and cardiac output predicts mortality in this and other classical rodent sepsis models.⁸⁴ At the T2 phase of CVB3 infection, we documented a PAR2- β -arrestin-mediated abrogation of LV filling. In contrast, LV dilation emerged in PAR2 cleavage-resistant mice at T2, at least partially resuscitating cardiac output. Similarly, LV dilation occurring in cecal ligation and puncture-induced septic shock mouse models or being apparent in human sepsis were associated with improved cardiovascular performance and survival.⁸⁵ Therefore, our findings highlight the importance of the PAR2- β -arrestin axis for control of diastolic filling during septic shock.

The findings in A/J mice, however, where inhibition of TF-FVIIa signaling by NAPc2 had no substantial effect on diastolic filling at T2 proves the biological relevance of other PAR2 stimulants that provoke the hypodynamic effects of distributive conditions in CVB3 infection. Nevertheless, we documented improved LV ejection fraction in NAPc2-treated mice presumably compensating the low output in infection, reminiscent of the hyperdynamic phase of sepsis with elevated systolic function. Correspondingly, we found less fluid retention in the lungs of NAPc2-treated mice, which can be attributed to improved forward function of the LV as well. Taken together, we identified the TF-FVIIa-PAR2- β -arrestin axis to provoke the negative impact of a viral infection on host health condition without directly affecting pathogen burden and defined blockade of TF-FVIIa as a therapeutic modality in this context.

ARTICLE INFORMATION

Received September 12, 2023; accepted February 5, 2024.

Affiliations

Institute of Biochemistry (M.K., C.B., N.K., S.P., A.B.), Department of Pediatrics, Division of Pulmonology, Immunology and Critical Care Medicine (C.C.G.), and Core Facility High-Throughput Mass Spectrometry (M.M.), Charité-Universitätsmedizin Berlin, Freie Universität Berlin and Humboldt-Universität zu Berlin, Germany. Clinician Scientist Program, BIH (Berlin Institute of Health) Academy, BIH, Charité-Universitätsmedizin Berlin, Germany (C.C.G.). Deutsches Herzzentrum der Charité, Institute of Computer-Assisted Cardiovascular Medicine, Berlin, Germany (N.B.). Charité-Universitätsmedizin Berlin, Freie Universität Berlin and Humboldt-Universität zu Berlin, Germany (N.B.). Deutsches Zentrum für Herz-Kreislauf-Forschung (DZHK), partner site Berlin, Germany (M.K., A.B.). Deutsches Zentrum für Herz-Kreislauf-Forschung (DZHK), partner site Rhein-Main, Germany (K.G., D.K., W.R.). German Rheumatism Research Center, Leibniz Association, Berlin, Germany (C.C.G.). German Federal Institute for Risk Assessment, Berlin, Germany (N.A.). Translational Oncology at the University Medical Center of the Johannes Gutenberg University Mainz (TRON), Germany (T.B., V.B.). University Medical Center Mainz, Center for Thrombosis and Hemostasis, Germany (K.G., D.K., W.R.). Max-Delbrueck-Center for Molecular Medicine, Animal Phenotyping Platform, Berlin, Germany (A.H.). University Hospital Tuebingen, Institute for Pathology and Neuropathology, Cardiopathology, Germany (M.S., K.K.). Versiti Blood Research Institute, Milwaukee, WI (H.W.). German Institute of Human Nutrition Potsdam-Rehbruecke, Department of Molecular Toxicology, Nuthetal, Germany (N.B.). University Medical Center Mainz, Institute for Pathology, Johannes-Gutenberg-Universität Mainz, Germany (M.M.G.). University Medical Center Mainz, Research Center for Immunotherapy, Johannes-Gutenberg-Universität Mainz, Germany (M.M.G.). Joint Unit Immunopathology, Institute of Pathology, University Medical Center, Johannes Gutenberg University of Mainz, Germany (M.M.G.). TRON, Mainz, Germany (M.M.G.).

Acknowledgments

The authors acknowledge Karolin Voss, Martin Taube, Prisca Kunert, Anika Linder, Bonny Adami, and Sandra Bundschuh for excellent technical assistance; Sabine Reyda and Guisya Carlino for mouse colony support; Daniela Ludwig for support in sample preparation; and Kathrin Textoris-Taube for analytical instrumentation. M. Gotthardt provided images for the schematic work flows. The authors acknowledge T. Kaiser and the support provided by the Flow Cytometry Core Facility of the German Rheumatism Research Center, Berlin, Germany.

Sources of Funding

A. Beling receives support from the Foundation for Experimental Biomedicine Zurich, Switzerland. Deutsche Forschungsgemeinschaft (German Research Foundation) supported this project (project identifier [ID] 318346496-CRC1292 [TP02] to A. Beling and W. Ruf and CRC1292 [TP001N] to M.M. Gaida and V. Bukur, project ID 259373024-TRR 167 [B16N] to A. Beling, project ID BE 6335/4-3 and BE 6335/5-1 to A. Beling, CRC1470 [A08] to A. Beling and N. Berndt). C. Bredow and M. Kespohl received support by International Max Planck Research School for Infectious Diseases and Immunology, Berlin. N. Berndt was supported by the German Research Foundation (project ID 422215721). C.C. Goetzke is a participant in the BIH (Berlin Institute of Health)-Charité Clinician Scientist Program funded by Charité-Universitätsmedizin Berlin and the Berlin Institute of Health.

Disclosures

The patent application EP21174633 with the title "Computer Assisted Method for the Evaluation of Cardiac Metabolism" was filed by Charité-Universitätsmedizin Berlin as the employer of N. Berndt and Titus Kuehne, with both holding inventorship for this patent application. The other authors report no conflicts.

Supplemental Material

Figures S1-S14

Tables S1-S4

Major Resources Table

REFERENCES

- Ebert J, Wilgenbus P, Teiber JF, Jurk K, Schwierczek K, Döhrmann M, Xia N, Li H, Spiecker L, Ruf W, et al. Paraoxonase-2 regulates coagulation activation through endothelial tissue factor. *Blood*. 2018;131:2161-2172. doi: 10.1182/blood-2017-09-807040
- Schaffner F, Versteeg HH, Schillert A, Yokota N, Petersen LC, Mueller BM, Ruf W. Cooperation of tissue factor cytoplasmic domain and PAR2 signaling in breast cancer development. *Blood*. 2010;116:6106-6113. doi: 10.1182/blood-2010-06-289314
- Antoniak S, Mackman N. Multiple roles of the coagulation protease cascade during virus infection. *Blood*. 2014;123:2605-2613. doi: 10.1182/blood-2013-09-526277
- Pawlinski R, Mackman N. Cellular sources of tissue factor in endotoxemia and sepsis. *Thromb Res*. 2010;125(suppl 1):S70-S73. doi: 10.1016/j.thromres.2010.01.042
- Rothmeier AS, Liu E, Chakrabarty S, Disse J, Mueller BM, Østergaard H, Ruf W. Identification of the integrin-binding site on coagulation factor VIIa required for proangiogenic PAR2 signaling. *Blood*. 2018;131:674-685. doi: 10.1182/blood-2017-02-768218
- Liang HP, Kerschen EJ, Hernandez I, Basu S, Zogg M, Botros F, Jia S, Hessner MJ, Griffin JH, Ruf W, et al. EPCR-dependent PAR2 activation by the blood coagulation initiation complex regulates LPS-triggered interferon responses in mice. *Blood*. 2015;125:2845-2854. doi: 10.1182/blood-2014-11-610717
- Disse J, Petersen HH, Larsen KS, Persson E, Esmon N, Esmon CT, Teyton L, Petersen LC, Ruf W. The endothelial protein C receptor supports tissue factor ternary coagulation initiation complex signaling through protease-activated receptors. *J Biol Chem*. 2011;286:5756-5767. doi: 10.1074/jbc.M110.201228
- Sutherland MR, Ruf W, Prydzial EL. Tissue factor and glycoprotein C on herpes simplex virus type 1 are protease-activated receptor 2 cofactors that enhance infection. *Blood*. 2012;119:3638-3645. doi: 10.1182/blood-2011-08-376814
- Geisbert TW, Hensley LE, Jahrling PB, Larsen T, Geisbert JB, Paragas J, Young HA, Fredeking TM, Rote WE, Vlasuk GP. Treatment of Ebola virus infection with a recombinant inhibitor of factor VIIa/tissue factor: a study in rhesus monkeys. *Lancet*. 2003;362:1953-1958. doi: 10.1016/S0140-6736(03)15012-X
- Nhu QM, Shirey K, Tejjaro JR, Farber DL, Netzel-Arnett S, Antalis TM, Fasano A, Vogel SN. Novel signaling interactions between proteinase-activated receptor 2 and toll-like receptors in vitro and in vivo. *Mucosal Immunol*. 2010;3:29-39. doi: 10.1038/mi.2009.120
- Rallabhandi P, Nhu QM, Toshchakov VY, Piao W, Medvedev AE, Hollenberg MD, Fasano A, Vogel SN. Analysis of proteinase-activated receptor 2 and TLR4 signal transduction: a novel paradigm for receptor cooperativity. *J Biol Chem*. 2008;283:24314-24325. doi: 10.1074/jbc.M804800200
- Nhu QM, Shirey KA, Pennini ME, Stiltz J, Vogel SN. Proteinase-activated receptor 2 activation promotes an anti-inflammatory and alternatively activated phenotype in LPS-stimulated murine macrophages. *Innate Immun*. 2012;18:193-203. doi: 10.1177/1753425910395044
- Whitton JL, Cornell CT, Feuer R. Host and virus determinants of picornavirus pathogenesis and tropism. *Nat Rev Microbiol*. 2005;3:765-776. doi: 10.1038/nrmicro1284
- Thibaut HJ, De Palma AM, Neyts J. Combating enterovirus replication: state-of-the-art on antiviral research. *Biochem Pharmacol*. 2012;83:185-192. doi: 10.1016/j.bcp.2011.08.016
- Negishi H, Osawa T, Ogami K, Ouyang X, Sakaguchi S, Koshiba R, Yanai H, Seko Y, Shitara H, Bishop K, et al. A critical link between toll-like receptor 3 and type II interferon signaling pathways in antiviral innate immunity. *Proc Natl Acad Sci USA*. 2008;105:20446-20451. doi: 10.1073/pnas.0810372105
- Riad A, Westermann D, Zietsch C, Savvatis K, Becher PM, Bereswill S, Heimesaat MM, Lettau O, Lassner D, Dörner A, et al. TRIF is a critical survival factor in viral cardiomyopathy. *J Immunol*. 2011;186:2561-2570. doi: 10.4049/jimmunol.1002029
- Deonarain R, Cerullo D, Fuse K, Liu PP, Fish EN. Protective role for interferon-beta in coxsackievirus B3 infection. *Circulation*. 2004;110:3540-3543. doi: 10.1161/01.CIR.0000136824.73458.20
- Gorbea C, Makar KA, Pauschinger M, Pratt G, Bersola JLF, Varela J, David RM, Banks L, Huang CH, Li H, et al. A role for toll-like receptor 3 variants in host susceptibility to enteroviral myocarditis and dilated cardiomyopathy. *J Biol Chem*. 2010;285:23206-23221. doi: 10.1074/jbc.M109.047464
- Rahnefeld A, Klingel K, Schuermann A, Diny NL, Althof N, Lindner A, Bleienheuff P, Savvatis K, Respondek D, Opitz E, et al. Ubiquitin-like protein ISG15 (interferon-stimulated gene of 15 kDa) in host defense against heart failure in a mouse model of virus-induced cardiomyopathy. *Circulation*. 2014;130:1589-1600. doi: 10.1161/CIRCULATIONAHA.114.009847
- Abston ED, Coronado MJ, Bucek A, Onyimba JA, Brandt JE, Frisancho JA, Kim E, Bedja D, Sung YK, Radtke AJ, et al. TLR3 deficiency induces chronic inflammatory cardiomyopathy in resistant mice following coxsackievirus B3 infection: role for IL-4. *Am J Physiol Regul Integr Comp Physiol*. 2013;304:R267-R277. doi: 10.1152/ajpregu.00516.2011
- Kimura T, Flynn CT, Alirezaei M, Sen GC, Whitton JL. Biphasic and cardiomyocyte-specific IFIT activity protects cardiomyocytes from enteroviral infection. *PLoS Pathog*. 2019;15:e1007674. doi: 10.1371/journal.ppat.1007674
- Althof N, Harkins S, Kemball CC, Flynn CT, Alirezaei M, Whitton JL. In vivo ablation of type I interferon receptor from cardiomyocytes delays coxsackievirus clearance and accelerates myocardial disease. *J Virol*. 2014;88:5087-5099. doi: 10.1128/JVI.00184-14
- Koestner W, Spanier J, Klause T, Tegtmeyer PK, Becker J, Herder V, Borst K, Todt D, Lienenklaus S, Gerhauser I, et al. Interferon-beta expression and type I interferon receptor signaling of hepatocytes prevent hepatic necrosis and virus dissemination in coxsackievirus B3-infected mice. *PLoS Pathog*. 2018;14:e1007235. doi: 10.1371/journal.ppat.1007235
- Kespohl M, Bredow C, Klingel K, Voss M, Paeschke A, Zickler M, Poller W, Kaya Z, Eckstein J, Fechner H, et al. Protein modification with ISG15 blocks coxsackievirus pathology by antiviral and metabolic reprogramming. *Sci Adv*. 2020;6:eaaay1109. doi: 10.1126/sciadv.aay1109
- Siednienko J, Gajanayake T, Fitzgerald KA, Moynagh P, Miggin SM. Absence of MyD88 results in enhanced TLR3-dependent phosphorylation of IRF3 and increased IFN- β and RANTES production. *J Immunol*. 2011;186:2514-2522. doi: 10.4049/jimmunol.1003093
- Fuse K, Chan G, Liu YA, Gudgeon P, Husain M, Chen MY, Yeh WC, Akira S, Liu PP. Myeloid differentiation factor-88 plays a crucial role in the pathogenesis of coxsackievirus B3-induced myocarditis and influences type I interferon production. *Circulation*. 2005;112:2276-2285. doi: 10.1161/CIRCULATIONAHA.105.536433
- Fairweather D, Yusing S, Frisancho S, Barrett M, Gatewood S, Steele R, Rose NR. IL-12 receptor beta 1 and toll-like receptor 4 increase IL-1 beta and IL-18-associated myocarditis and coxsackievirus replication. *J Immunol*. 2003;170:4731-4737. doi: 10.4049/jimmunol.170.9.4731
- Antoniak S, Owens AP 3rd, Baunacke M, Williams JC, Lee RD, Weithaus A, Sheridan PA, Malz R, Luyendyk JP, Esserman DA, et al.

- PAR-1 contributes to the innate immune response during viral infection. *J Clin Invest*. 2013;123:1310–1322. doi: 10.1172/JCI66125
29. Weithäuser A, Bobbert P, Antoniak S, Bohm A, Rauch BH, Klingel K, Savvatis K, Kroemer HK, Tschope C, Stroux A, et al. Protease-activated receptor-2 regulates the innate immune response to viral infection in a coxsackievirus B3-induced myocarditis. *J Am Coll Cardiol*. 2013;62:1737–1745. doi: 10.1016/j.jacc.2013.05.076
 30. Bochenek ML, Gogiraju R, Großmann S, Krug J, Orth J, Reyda S, Georgiadis GS, Spronk HM, Konstantinides S, Münzel T, et al. EPCR-PAR1 biased signaling regulates perfusion recovery and neovascularization in peripheral ischemia. *JCI Insight*. 2022;7:e157701. doi: 10.1172/jci.insight.157701
 31. Müller-Calleja N, Hollerbach A, Ritter S, Pedrosa DG, Strand D, Graf C, Reinhardt C, Strand S, Poncelet P, Griffin JH, et al. Tissue factor pathway inhibitor primes monocytes for antiphospholipid antibody-induced thrombosis. *Blood*. 2019;134:1119–1131. doi: 10.1182/blood.2019001530
 32. Perez-Riverol Y, Bai J, Bandla C, García-Seisdedos D, Hewapathirana S, Kamatchinathan S, Kundu DJ, Prakash A, Frericks-Zipper A, Eisenacher M, et al. The PRIDE database resources in 2022: a hub for mass spectrometry-based proteomics evidences. *Nucleic Acids Res*. 2022;50:D543–D552. doi: 10.1093/nar/gkab1038
 33. Klingel K, Hohenadl C, Canu A, Albrecht M, Seemann M, Mall G, Kandolf R. Ongoing enterovirus-induced myocarditis is associated with persistent heart-muscle infection - quantitative-analysis of virus-replication, tissue-damage, and inflammation. *Proc Natl Acad Sci USA*. 1992;89:314–318. doi: 10.1073/pnas.89.1.314
 34. Knowlton KU, Jeon ES, Berkley N, Wessely R, Huber S. A mutation in the puff region of VP2 attenuates the myocarditic phenotype of an infectious cDNA of the Woodruff variant of coxsackievirus B3. *J Virol*. 1996;70:7811–7818. doi: 10.1128/JVI.70.11.7811-7818.1996
 35. Larsen KS, Ostergaard H, Olsen OH, Bjelke JR, Ruf W, Petersen LC. Engineering of substrate selectivity for tissue factor-factor VIIa complex signaling through protease-activated receptor 2. *J Biol Chem*. 2010;285:19959–19966. doi: 10.1074/jbc.M110.101030
 36. Graf C, Wilgenbus P, Pagel S, Pott J, Marini F, Reyda S, Kitano M, Macher-Goppinger S, Weiler H, Ruf W. Myeloid cell-synthesized coagulation factor X dampens antitumor immunity. *Sci Immunol*. 2019;4:eaaw8405. doi: 10.1126/sciimmunol.aaw8405
 37. DeFea KA, Zalevsky J, Thoma MS, Dery O, Mullins RD, Bunnett NW. Beta-arrestin-dependent endocytosis of proteinase-activated receptor 2 is required for intracellular targeting of activated ERK1/2. *J Cell Biol*. 2000;148:1267–1281. doi: 10.1083/jcb.148.6.1267
 38. Zelaya H, Grunz K, Nguyen TS, Habibi A, Witzler CL, Reyda S, Gonzalez-Menendez I, Quintanilla-Martinez L, Bosmann M, Weiler H, et al. Nucleic acid sensing promotes inflammatory monocyte migration through biased coagulation factor VIIa signaling [published online December 14, 2023]. *Blood*. doi: 10.1182/blood.2023021149
 39. Bergum PW, Cruikshank A, Maki SL, Kelly CR, Ruf W, Vlasuk GP. Role of zymogen and activated factor X as scaffolds for the inhibition of the blood coagulation factor VIIa-tissue factor complex by recombinant nematode anticoagulant protein c2. *J Biol Chem*. 2001;276:10063–10071. doi: 10.1074/jbc.M009116200
 40. Veteläinen RL, Bennis RJ, de Bruin K, van Vliet A, van Gulik TM. Hepatobiliary function assessed by 99mTc-mebrofenin cholescintigraphy in the evaluation of severity of steatosis in a rat model. *Eur J Nucl Med Mol Imaging*. 2006;33:1107–1114. doi: 10.1007/s00259-006-0125-3
 41. Zhang Q, Zhang P, Li B, Dang H, Jiang J, Meng L, Zhang H, Zhang Y, Wang X, Li Q, et al. The expression of perilipin family proteins can be used as diagnostic markers of liposarcoma and to differentiate subtypes. *J Cancer*. 2020;11:4081–4090. doi: 10.7150/jca.41736
 42. Althof N, Goetzke CC, Kespohl M, Voss K, Heuser A, Pinkert S, Kaya Z, Klingel K, Beling A. The immunoproteasome-specific inhibitor ONX 0914 reverses susceptibility to acute viral myocarditis. *EMBO Mol Med*. 2018;10:200–218. doi: 10.15252/emmm.201708089
 43. Pinkert S, Kespohl M, Kelm N, Kaya Z, Heuser A, Klingel K, Beling A. Exploration of analgesia with tramadol in the coxsackievirus B3 myocarditis mouse model. *Viruses*. 2021;13:1222. doi: 10.3390/v13071222
 44. R Core Team. *A Language and Environment for Statistical Computing*. R Foundation for Statistical Computing; 2017. <https://www.R-project.org/>
 45. Dvinge H, Bertone P. HTqPCR: high-throughput analysis and visualization of quantitative real-time PCR data in R. *Bioinformatics*. 2009;25:3325–3326. doi: 10.1093/bioinformatics/btp578
 46. Ritchie ME, Phipson B, Wu D, Hu Y, Law CW, Shi W, Smyth GK. limma powers differential expression analyses for RNA-sequencing and microarray studies. *Nucleic Acids Res*. 2015;43:e47. doi: 10.1093/nar/gkv007
 47. Müller T, Kalxdorf M, Longuespée R, Kazdal DN, Stenzinger A, Krijgsveld J. Automated sample preparation with SP3 for low-input clinical proteomics. *Mol Syst Biol*. 2020;16:e9111. doi: 10.15252/msb.20199111
 48. Demichev V, Messner CB, Vernardis SI, Lilley KS, Ralser M. DIA-NN: neural networks and interference correction enable deep proteome coverage in high throughput. *Nat Methods*. 2020;17:41–44. doi: 10.1038/s41592-019-0638-x
 49. UniProt Consortium. UniProt: the universal protein knowledgebase in 2021. *Nucleic Acids Res*. 2021;49:D480–d489. doi: 10.1093/nar/gkaa1100
 50. Ashburner M, Ball CA, Blake JA, Botstein D, Butler H, Cherry JM, Davis AP, Dolinski K, Dwight SS, Eppig JT, et al. Gene ontology: tool for the unification of biology. The Gene Ontology Consortium. *Nat Genet*. 2000;25:25–29. doi: 10.1038/75556
 51. The Gene Ontology Consortium. Expansion of the Gene Ontology knowledgebase and resources. *Nucleic Acids Res*. 2017;45:D331–D338. doi: 10.1093/nar/gkw1108
 52. Mi H, Muruganujan A, Ebert D, Huang X, Thomas PD. PANTHER version 14: more genomes, a new PANTHER GO-slim and improvements in enrichment analysis tools. *Nucleic Acids Res*. 2019;47:D419–D426. doi: 10.1093/nar/gky1038
 53. Berndt N, Bulik S, Wallach I, Wunsch T, König M, Stockmann M, Meierhofer D, Holzhütter HG. HEPATOKIN1 is a biochemistry-based model of liver metabolism for applications in medicine and pharmacology. *Nat Commun*. 2018;9:2386. doi: 10.1038/s41467-018-04720-9
 54. Malz R, Weithäuser A, Tschöpe C, Schultheiss HP, Rauch U. Inhibition of coagulation factor Xa improves myocardial function during CVB3-induced myocarditis. *Cardiovasc Ther*. 2014;32:113–119. doi: 10.1111/1755-5922.12069
 55. Goetzke CC, Althof N, Neumaier HL, Heuser A, Kaya Z, Kespohl M, Klingel K, Beling A. Mitigated viral myocarditis in A/J mice by the immunoproteasome inhibitor ONX 0914 depends on inhibition of systemic inflammatory responses in coxsackievirusB3 infection. *Basic Res Cardiol*. 2021;116:7. doi: 10.1007/s00395-021-00848-w
 56. Pinkert S, Pryshliak M, Pappritz K, Knoch K, Hazini A, Dieringer B, Schaar K, Dong F, Hinze L, Lin J, et al. Development of a new mouse model for coxsackievirus-induced myocarditis by attenuating coxsackievirus B3 virulence in the pancreas. *Cardiovasc Res*. 2020;116:1756–1766. doi: 10.1093/cvr/cvz259
 57. Kallewaard NL, Zhang L, Chen JW, Guttenberg M, Sanchez MD, Bergelson JM. Tissue-specific deletion of the coxsackievirus and adenovirus receptor protects mice from virus-induced pancreatitis and myocarditis. *Cell host & microbe*. 2009;6:91–98. doi: 10.1016/j.chom.2009.05.018
 58. Kimura T, Flynn CT, Whitton JL. Hepatocytes trap and silence coxsackieviruses, protecting against systemic disease in mice. *Commun Biol*. 2020;3:580. doi: 10.1038/s42003-020-01303-7
 59. Wu D, Sanin DE, Everts B, Chen Q, Qiu J, Buck MD, Patterson A, Smith AM, Chang CH, Liu Z, et al. Type 1 interferons induce changes in core metabolism that are critical for immune function. *Immunity*. 2016;44:1325–1336. doi: 10.1016/j.immuni.2016.06.006
 60. Baaten BJ, Tinoco R, Chen AT, Bradley LM. Regulation of antigen-experienced T cells: lessons from the quintessential memory marker CD44. *Front Immunol*. 2012;3:23. doi: 10.3389/fimmu.2012.00023
 61. Buddai SK, Touloukhonova L, Bergum PW, Vlasuk GP, Krishnaswamy S. Nematode anticoagulant protein c2 reveals a site on factor Xa that is important for macromolecular substrate binding to human prothrombinase. *J Biol Chem*. 2002;277:26689–26698. doi: 10.1074/jbc.M202507200
 62. Kamikubo Y, Mendolicchio GL, Zampolli A, Marsechese P, Rothmeier AS, Orje JN, Gale AJ, Krishnaswamy S, Gruber A, Østergaard H, et al. Selective factor VIII activation by the tissue factor-factor VIIa-factor Xa complex. *Blood*. 2017;130:1661–1670. doi: 10.1182/blood-2017-02-767079
 63. Riewald M, Ruf W. Mechanistic coupling of protease signaling and initiation of coagulation by tissue factor. *Proc Natl Acad Sci USA*. 2001;98:7742–7747. doi: 10.1073/pnas.141126698
 64. Badeanlou L, Furlan-Freguia C, Yang G, Ruf W, Samad F. Tissue factor-protease-activated receptor 2 signaling promotes diet-induced obesity and adipose inflammation. *Nat Med*. 2011;17:1490–1497. doi: 10.1038/nm.2461
 65. Garlapati V, Molitor M, Michna T, Harms GS, Finger S, Jung R, Lagrange J, Efentakis P, Wild J, Knorr M, et al. Targeting myeloid cell coagulation signaling blocks MAP kinase/TGF-β1-driven fibrotic remodeling in ischemic heart failure. *J Clin Invest*. 2023;133:e156436. doi: 10.1172/JCI156436
 66. Antoniak S, Boltzen U, Riad A, Kallwells-Opara A, Rohde M, Dorner A, Tschope C, Noutsias M, Pauschinger M, Schultheiss HP, et al. Viral myocarditis and coagulopathy: increased tissue factor expression and plasma thrombogenicity. *J Mol Cell Cardiol*. 2008;45:118–126. doi: 10.1016/j.jmcc.2008.03.013

67. Geisbert TW, Young HA, Jahrling PB, Davis KJ, Kagan E, Hensley LE. Mechanisms underlying coagulation abnormalities in ebola hemorrhagic fever: overexpression of tissue factor in primate monocytes/macrophages is a key event. *J Infect Dis*. 2003;188:1618–1629. doi: 10.1086/379724
68. Zelaya H, Rothmeier AS, Ruf W. Tissue factor at the crossroad of coagulation and cell signaling. *J Thromb Haemost*. 2018;16:1941–1952. doi: 10.1111/jth.14246
69. Hess CN, Hsia J, Carroll IA, Nehler MR, Ruf W, Morrow DA, Nicolau JC, Berwanger O, Szarek M, Capell WH, et al. Novel tissue factor inhibition for thromboprophylaxis in COVID-19: primary results of the ASPEN-COVID-19 trial. *Arterioscler Thromb Vasc Biol*. 2023;43:1572–1582. doi: 10.1161/ATVBAHA.122.318748
70. Saffarzadeh M, Grunz K, Nguyen TS, Lee YK, Kitano M, Danckwardt S, Rodrigues CDS, Weiler H, Reyda S, Ruf W. Macrophage protease-activated receptor 2 regulates fetal liver erythropoiesis in mice. *Blood Adv*. 2020;4:5810–5824. doi: 10.1182/bloodadvances.2020003299
71. Bockstahler M, Fischer A, Goetzke CC, Neumaier HL, Sauter M, Kespohl M, Müller AM, Meckes C, Salbach C, Schenk M, et al. Heart-specific immune responses in an animal model of autoimmune-related myocarditis mitigated by an immunoproteasome inhibitor and genetic ablation. *Circulation*. 2020;141:1885–1902. doi: 10.1161/CIRCULATIONAHA.119.043171
72. Beling A, Kespohl M. Proteasomal protein degradation: adaptation of cellular proteolysis with impact on virus- and cytokine-mediated damage of heart tissue during myocarditis. *Front Immunol*. 2018;9:2620. doi: 10.3389/fimmu.2018.02620
73. Corsten MF, Schroen B, Heymans S. Inflammation in viral myocarditis: friend or foe? *Trends Mol Med*. 2012;18:426–437. doi: 10.1016/j.molmed.2012.05.005
74. Neumaier HL, Harel S, Klingel K, Kaya Z, Heuser A, Kespohl M, Beling A. ONX 0914 lacks selectivity for the cardiac immunoproteasome in coxsackievirus B3 myocarditis of NMRI mice and promotes virus-mediated tissue damage. *Cells*. 2020;9:1093. doi: 10.3390/cells9051093
75. Paeschke A, Possehl A, Klingel K, Voss M, Voss K, Kespohl M, Sauter M, Overkleef HS, Althof N, Garlanda C, et al. The immunoproteasome controls the availability of the cardioprotective pattern recognition molecule Pentraxin3. *Eur J Immunol*. 2016;46:619–633. doi: 10.1002/eji.201545892
76. Luo H, Yanagawa B, Zhang J, Luo Z, Zhang M, Esfandiarei M, Carthy C, Wilson JE, Yang D, McManus BM. Coxsackievirus B3 replication is reduced by inhibition of the extracellular signal-regulated kinase (ERK) signaling pathway. *J Virol*. 2002;76:3365–3373. doi: 10.1128/jvi.76.7.3365-3373.2002
77. Schmidt C, Berger T, Groettrup M, Basler M. Immunoproteasome inhibition impairs T and B cell activation by restraining ERK signaling and proteostasis. *Front Immunol*. 2018;9:2386. doi: 10.3389/fimmu.2018.02386
78. Shearer AM, Wang Y, Fletcher EK, Rana R, Michael ES, Nguyen N, Abdelmalek MF, Covic L, Kuliopulos A. PAR2 promotes impaired glucose uptake and insulin resistance in NAFLD through GLUT2 and Akt interference. *Hepatology*. 2022;76:1778–1793. doi: 10.1002/hep.32589
79. Rana R, Shearer AM, Fletcher EK, Nguyen N, Guha S, Cox DH, Abdelmalek M, Wang Y, Baleja JD, Covic L, et al. PAR2 controls cholesterol homeostasis and lipid metabolism in nonalcoholic fatty liver disease. *Mol Metab*. 2019;29:99–113. doi: 10.1016/j.molmet.2019.08.019
80. Hara T, Phuong PT, Fukuda D, Yamaguchi K, Murata C, Nishimoto S, Yagi S, Kusunose K, Yamada H, Soeki T, et al. Protease-activated receptor-2 plays a critical role in vascular inflammation and atherosclerosis in apolipoprotein E-deficient mice. *Circulation*. 2018;138:1706–1719. doi: 10.1161/CIRCULATIONAHA.118.033544
81. Wang J, Chakrabarty S, Bui Q, Ruf W, Samad F. Hematopoietic tissue factor-protease-activated receptor 2 signaling promotes hepatic inflammation and contributes to pathways of gluconeogenesis and steatosis in obese mice. *Am J Pathol*. 2015;185:524–535. doi: 10.1016/j.ajpath.2014.10.008
82. Laufman O, Perrino J, Andino R. Viral generated inter-organelle contacts redirect lipid flux for genome replication. *Cell*. 2019;178:275–289.e16. doi: 10.1016/j.cell.2019.05.030
83. Laitano O, Van Steenberg D, Mattingly AJ, Garcia CK, Robinson GP, Murray KO, Clanton TL, Nunamaker EA. Xiphoid surface temperature predicts mortality in a murine model of septic shock. *Shock*. 2018;50:226–232. doi: 10.1097/SHK.0000000000001007
84. Hoffman M, Kyriazis ID, Lucchese AM, de Lucia C, Piedepalumbo M, Bauer M, Schulze PC, Bonios MJ, Koch WJ, Drosatos K. Myocardial strain and cardiac output are preferable measurements for cardiac dysfunction and can predict mortality in septic mice. *J Am Heart Assoc*. 2019;8:e012260. doi: 10.1161/JAHA.119.012260
85. Zanotti Cavazzoni SL, Guglielmi M, Parrillo JE, Walker T, Dellinger RP, Hollenberg SM. Ventricular dilation is associated with improved cardiovascular performance and survival in sepsis. *Chest*. 2010;138:848–855. doi: 10.1378/chest.09-1086